

¹ Study of the multi-strange resonance $\Xi(1530)^0$ production
² with ALICE at the LHC energies

³ Jihye Song

4 Contents

5	List of Figures	4
6	List of Tables	8
7	1 The physics of relativistic heavy-ion collisions	9
8	1.1 Standard model	9
9	1.2 Quantum Chromo-Dynamics	9
10	1.3 Heavy Ion Collisions	9
11	2 Production of resonance with strangeness	9
12	2.1 Resonance with strangeness	9
13	3 Theoretical models	9
14	3.1 Thermal statistical model	9
15	3.1.1 Calculations	11
16	3.1.2 Results	11
17	3.1.3 Comparison with data	13
18	3.2 UrQMD	13
19	4 A Large Ion Collider Experiment at the LHC	13
20	4.1 The Large Hadron Collider	14
21	4.2 The ALICE project	14
22	4.2.1 ALICE detector	14
23	4.2.2 Data Acquisition (DAQ) and trigger system	14
24	4.2.3 ALICE offline software frame work	14
25	5 Measurement of $\Xi(1530)^0$ production in p-Pb and Pb-Pb	14
26	5.1 $\Xi(1530)^0$ -reconstruction	15
27	5.1.1 Data sample and event selection	15
28	5.1.2 Track and topological selection	18
29	5.1.3 Particle identification	21
30	5.1.4 Signal extraction	24
31	5.2 Efficiency correction	33
32	5.3 Corrected p_T -spectra	36
33	5.4 Systematic uncertainties	38
34	5.5 $\Xi(1530)^0$ transverse momentum spectra	43
35	6 Further results and discussion	46
36	6.1 Mean transverse momentum	46
37	6.2 Particle yield ratios	50

38	6.2.1 Integrated yield ratios of excited to ground-state hadrons	50
39	6.3 Integrated yield ratios to pion	53
40	References	57

⁴¹ **List of Figures**

42	1	Ratio of baryonic and mesonic resonances over their stable partner as a function of temperature.	12
43	2	Ratio of resonances over their stable partner as a function of $\sqrt(s)$	13
44	3	Vertex-z coordinate distribution of the accepted events in p–Pb collision(Left) and in Pb–Pb collisions(Right). The red dashed line indicates vertex cut .	16
45	4	Multiplicity distribution of accepted events in p–Pb collision in percentile. The each color and labels define the four intervals in which the analysis is performed.	17
46	5	Centrality distribution of three different trigger classes.	18
47	6	Sketch of the decay modes for Ξ^{*0} and depiction of the track and topological selection criteria.	20
48	7	TPC dE/dx as function of transverse momentum for total (top) and selected first emitted π in 3σ (bottom)	21
49	8	TPC dE/dx as function of transverse momentum for total (top) and selected second emitted π in 3σ (bottom)	21
50	9	TPC dE/dx as function of transverse momentum for total (top) and selected last emitted π in 3σ (bottom)	22
51	10	TPC dE/dx as function of transverse momentum for total (top) and selected proton in 3σ (bottom)	22
52	11	TPC dE/dx as function of transverse momentum for total (top) and selected first emitted π in 3σ (bottom)	22
53	12	TPC dE/dx as function of transverse momentum for total (top) and selected second emitted π in 3σ (bottom)	23
54	13	TPC dE/dx as function of transverse momentum for total (top) and selected last emitted π in 3σ (bottom)	23
55	14	TPC dE/dx as function of transverse momentum for total (top) and selected proton in 3σ (bottom)	24
56	15	The $\Xi^\mp\pi^\pm$ invariant mass distribution (Same-event pairs) in $1.8 < p_T < 2.2 \text{ GeV}/c$ and for the multiplicity class 20-40%. The background shape, using pairs from different events (Mixed-event background), is normalised to the counts in $1.49 < M_{\Xi\pi} < 1.51 \text{ GeV}/c^2$ and $1.56 < M_{\Xi\pi} < 1.58 \text{ GeV}/c^2$	25
57	16	The $\Xi^\mp\pi^\pm$ invariant mass distribution (Same-event pairs) in $3.0 < p_T < 3.5 \text{ GeV}/c$ and for the centrality class 0-10%. The background shape, using pairs from different events (Mixed-event background), is normalised to the counts in $1.49 < M_{\Xi\pi} < 1.51 \text{ GeV}/c^2$ and $1.56 < M_{\Xi\pi} < 1.58 \text{ GeV}/c^2$	26
58	17	The invariant mass distribution after subtraction of the mixed-event background in p–Pb collisions. The solid curve represents the combined fit, while the dashed line describes the residual background.	27

80	18	The invariant mass distribution after subtraction of the mixed-event background in Pb–Pb collisions. The solid curve represents the combined fit, while the dashed line describes the residual background.	28
81	19	σ fit parameters as a function of p_{T} in MB in p–Pb collisions (top) and in Pb–Pb collisions (bottom).	30
82	20	$\Xi(1530)^0$ -mass obtained from fit of the Voigtian peak as a function of p_{T} in each multiplicity classes in p–Pb collisions (top) and the different centrality classes in Pb–Pb (bottom).	31
83	21	$\Xi(1530)^0$ -raw spectra obtained from fit of the Voigtian peak and a polynomial residual background for different multiplicities in p–Pb collisions (top) and Pb–Pb collisions (bottom). Only the statistical error is reported.	32
84	22	$\Xi(1530)^0$ -raw spectra obtained from fit of the Voigtian peak and a polynomial residual background for different multiplicities. Only the statistical error is reported.	33
85	23	Real corrected $\Xi(1530)^0$ spectrum (black) for the minimum bias with Levy fit (black curve). Also shown are the unweighted generated (blue) and reconstructed (red) $\Xi(1530)^0$ spectra.	34
86	24	Efficiency as a function of p_{T} in minimum bias events in p–Pb collisions.	35
87	25	Efficiency as a function of p_{T} in different centrality classes in Pb–Pb collisions	36
88	26	Corrected p_{T} -spectra of $\Xi(1530)^0$ in NSD and different multiplicity classes in p–Pb collisions.	37
89	27	Corrected p_{T} -spectra of $\Xi(1530)^0$ in different centrality classes in Pb–Pb collisions.	37
90	28	Summary of the contributions to the systematic uncertainty in minimum bias events in p–Pb collisions. The dashed black line is the sum in quadrature of all the contributions.	41
91	29	Systematic uncertainties for each multiplicity classes in p–Pb collisions.	41
92	30	Summary of the contributions to the systematic uncertainty in minimum bias events in Pb–Pb collisions. The dashed black line is the sum in quadrature of all the contributions.	42
93	31	Systematic uncertainties for each multiplicity classes.	42
94	32	Corrected yields as function of p_{T} in NSD events and multiplicity dependent event classes in p–Pb collision system. Statistical uncertainties are presented as bar and systematical uncertainties are plotted as boxes.	44
95	33	Corrected yields as function of p_{T} in different centrality classes in Pb–Pb collision system. Statistical uncertainties are presented as bar and systematical uncertainties are plotted as boxes.	45

117	34	Mean transverse momenta $\langle p_T \rangle$ of Λ , Ξ^- , $\Sigma^{*\pm}$, Ξ^{*0} and Ω^- in p–Pb collisions at $\sqrt{s_{NN}} = 5.02$ TeV as a function of mean charged-particle multiplicity density $\langle dN_{ch}/d\eta_{lab} \rangle$, measured in the pseudorapidity range $ \eta_{lab} < 0.5$. The results for Λ , Ξ^- and Ω^- are taken from [1, 2, 3]. Statistical and systematic uncertainties are represented as bars and boxes, respectively. The Ω^- and Ξ^- points in the 3rd and 4th lowest multiplicity bins are slightly displaced along the abscissa to avoid superposition with the $\Xi(1530)^0$ points.	47
124	35	Mass dependence of the mean transverse momenta of identified particles for the 0 – 20% V0A multiplicity class and with $-0.5 < y_{CMS} < 0$ in p–Pb collisions at $\sqrt{s_{NN}} = 5.02$ TeV [1, 3], and in minimum-bias pp collisions at $\sqrt{s} = 7$ TeV [4] with $ y_{CMS} < 0.5$. Additionally, D^0 and J/ψ results are plotted. The D^0 and J/ψ were measured in different rapidity ranges: $ y_{CMS} < 0.5$ [5] ($ y_{CMS} < 0.9$ [6]) for D^0 (J/ψ) in pp and $-0.96 < y_{CMS} < 0.04$ [5] ($-1.37 < y_{CMS} < 0.43$ [7]) for D^0 (J/ψ) in p–Pb. Note also that the results for D^0 and J/ψ in p–Pb collisions are for the 0–100% multiplicity class.	48
133	36	Ratio of $\Xi(1530)^0$ to Ξ^- measured in pp [4], p–Pb [1, 3] and Pb–Pb collisions as a function of $\langle dN_{ch}/d\eta_{lab} \rangle$ measured at midrapidity. Statistical uncertainties (bars) are shown as well as total systematic uncertainties (hollow boxes) and systematic uncertainties uncorrelated across multiplicity (shaded boxes). A few model predictions are also shown as lines at their appropriate abscissa.	51
139	37	Ratio of ρ/π (Up), K^*/K , ϕ/K (Left bottom) and Λ^*/Λ with system size measured at mid-rapidity. Statistical uncertainties (bars) are shown as well as total systematic uncertainties (hollow boxes) and systematic uncertainties uncorrelated across multiplicity (shaded boxes). A few model predictions are also shown as lines at their appropriate abscissa.	52
144	38	Ratio of $\Xi(1530)^0$ to π^\pm , measured in pp [8] and p–Pb [4] collisions, as a function of the average charged particle density ($\langle dN_{ch}/d\eta_{lab} \rangle$) measured at mid-rapidity. Statistical uncertainties (bars) are shown as well as total systematic uncertainties (hollow boxes) and systematic uncertainties uncorrelated across multiplicity (shaded boxes). A few model predictions are also shown as lines at their appropriate abscissa.	54
150	39	Particle yield ratios to pions of strange and multi-strange hadrons normalized to the values measured in pp collisions, both in pp and in p–Pb collisions. The common systematic uncertainties cancel in the double-ratio. The empty boxes represent the remaining uncorrelated uncertainties. The lines represent a simultaneous fit of the results with the empirical scaling formula in Equation ???.	55

156	40	p_T -integrated yield ratios of strange and multi-strange hadrons to $(\pi^+ + \pi^-)$		
157		as a function of $\langle dN_{ch}/d\eta_{lab} \rangle$ measured in the rapidity interval $ \eta < 0.5$. The		
158		empty and dark-shaded boxes show the total systematic uncertainty and the		
159		contribution uncorrelated across multiplicity bins, respectively. The values		
160		are compared to calculations from MC models and to results obtained in		
161		Pb–Pb and p–Pb collisions at the LHC.		56

¹⁶² **List of Tables**

163	1	Parameters used in the thermal-model calculations.	10
164	2	Properties of particles used in the ratio calculations.	11
165	3	Difference of mass (ΔM), baryon number (ΔB), strangeness (ΔS) and charge (ΔQ) of the ratios. The values of the slopes needs to be checked!!!! .	13
166	4	Number of accepted and analyzed events per multiplicity/centrality interval	18
167	5	Track selections common to all decay daughters and primary track selections applied to the charged pions from decays of Ξ^{*0}	19
169	6	Topological and track selection criteria.	19
170	7	Summary of the systematic uncertainties on the differential yield, $d^2N/(dp_T dy)$. Minimum and maximum values in all p_T intervals and multiplicity classes in p–Pb, centrality classes in Pb–Pb are shown for each source.	43
172			
173			

174 **1 The physics of relativistic heavy-ion collisions**

175 This test for references [9]

176 **1.1 Standard model**

177 **1.2 Quantum Chromo-Dynamics**

178 **1.3 Heavy Ion Collisions**

179 **2 Production of resonance with strangeness**

180 **2.1 Resonance with strangeness**

181 **3 Theoretical models**

182 **3.1 Thermal statistical model**

183 The statistical-thermal model has proved extremely successful in applications to relativistic
184 collisions of both heavy ions and elementary particles. In light of this success, THERMUS,
185 a thermal model analysis package, has been developed for incorporation into the object-
186 oriented ROOT framework [10].

187
188 There are three types of statistical-thermal models in explaining data in high energy nu-
189 clear physics and THERMUS treats the system quantum numbers B (baryon number), S
190 (strangeness) and Q (charge) within three distinct formalisms:

191 1. **Grand-Canonical Ensemble:** Because the hot dense matter produced in nucleus-
192 nucleus collisions is large enough, this ensemble is the most widely used in applications
193 to heavy-ion collisions, in which the quantum numbers are conserved on average.

194 2. **Fully-Canonical Ensemble:** In which B, S and Q are each exactly conserved and
195 this ensemble used in high-energy elementary collisions such as pp, p \bar{p} and e $^-$ e $^+$
196 collisions.

197 3. **Strangeness-Canonical Ensemble:** In small systems or at low temperatures, a
198 canonical treatment leads to a suppression of hadrons carrying non-zero quantum
199 numbers, since these particles have to be created in pairs and the resulting low
200 production of strange particles requires a canonical treatment of strangeness.

201 In order to calculate the thermal properties of a system, one starts with an evaluation
202 of its partition function. The form of the partition function obviously depends on the
203 choice of ensemble. In the present analysis the strangeness-canonical ensemble used and
204 the statistical-thermal model requires six parameters as input: the chemical freeze-out

205 temperature T , baryon and charge chemical potentials μ_B and μ_Q respectively, canonical
206 or correlation radius, R_C ; the radius inside which strangeness is exactly conserved and the
207 fireball radius R . An additional strangeness saturation factor γ_S has been used as indicator
208 of a possible departure from equilibrium and $\gamma_S = 1.0$ corresponds to complete strangeness
209 equilibration.

210 The volume dependence cancels out when studying the particle ratios as well as strangeness
211 canonical equivalent to grand canonical formalism if $\Delta S = 0$ in the ratios and γ_S also can-
212 cels out. Parameters used in the analysis listed in Table 1. The μ_B parameter taken from
213 the Ref. [11].

Table 1: Parameters used in the thermal-model calculations.

Parameter	Value
T (MeV)	varied (see text)
μ_B (MeV)	$9.2 \times 10^{-2}????$
μ_Q (MeV)	0.0
γ_S	1.0

215 **3.1.1 Calculations**

216 *Concept:*

217 In order to calculate the particle ratios within strangeness canonical formalism of THER-
 218 MUS, temperature varied between 60 MeV to 180 MeV and particle yields extracted for
 219 each temperature value and then primary particle ratios calculated for each case.

220

221 *Feed-Down Correction:*

222 Since the particle yields measured by the detectors in collision experiments include feed-
 223 down from heavier hadrons and hadronic resonances, the primordial hadrons are allowed to
 224 decay to particles considered stable by the experiment before model predictions are com-
 225 compared with experimental data. In the analysis only Λ particles counted as stable (do not
 226 allowed to decay) so there is no feed-down contribution from these particles to the other
 227 ratios.

228

229

230 Properties of studied particles and their particle ratios listed in Table 2 and Table 3,
 231 respectively.

Table 2: Properties of particles used in the ratio calculations.

Particle	Δ^{++}	p	K^{*0}	K^0	K^+	Λ^*	Λ	Σ^{*+}	Σ^+	Σ^0
Mass (MeV/c^2)	1232	938.27	895.92	497.61	493.67	1519.5	1115.68	1382.8	1189.37	1192.6
Width (MeV/c^2)	120	–	50.7	–	–	15.6	–	37.6	–	–
$c\tau$ (fm)	1.6	–	3.9	–	–	12.6	–	5.51	–	–
Ang. Momentum (J)	3/2	1/2	1	1	0	3/2	1/2	3/2	1/2	1/2
Isospin (I)	3/2	1/2	1/2	1/2	1/2	0	0	1	1	1
Parity (P)	+1	+1	-1	-1	0	-1	+1	+1	+1	+1
Strangeness (S)	0	0	1	1	1	-1	-1	-1	-1	-1
Baryon Number (B)	1	1	0	0	0	1	1	1	1	1
Decay Channel	$p\pi^+$	–	π^-	–	$\mu^+\nu_\mu$	pK^-	$p\pi^-$	$\Lambda\pi^+$	$p\pi^0$	$\Lambda\gamma$
Branching Ratio (%)	~ 100	–	~ 66.7	–	~ 63.54	~ 45	~ 63.9	~ 87	~ 51.6	~ 100
Q-Value(MeV/c^2)	154.16	–	262.68	–	–	87.55	37.84	127.55	111.53	76.96

232

233

234 **3.1.2 Results**

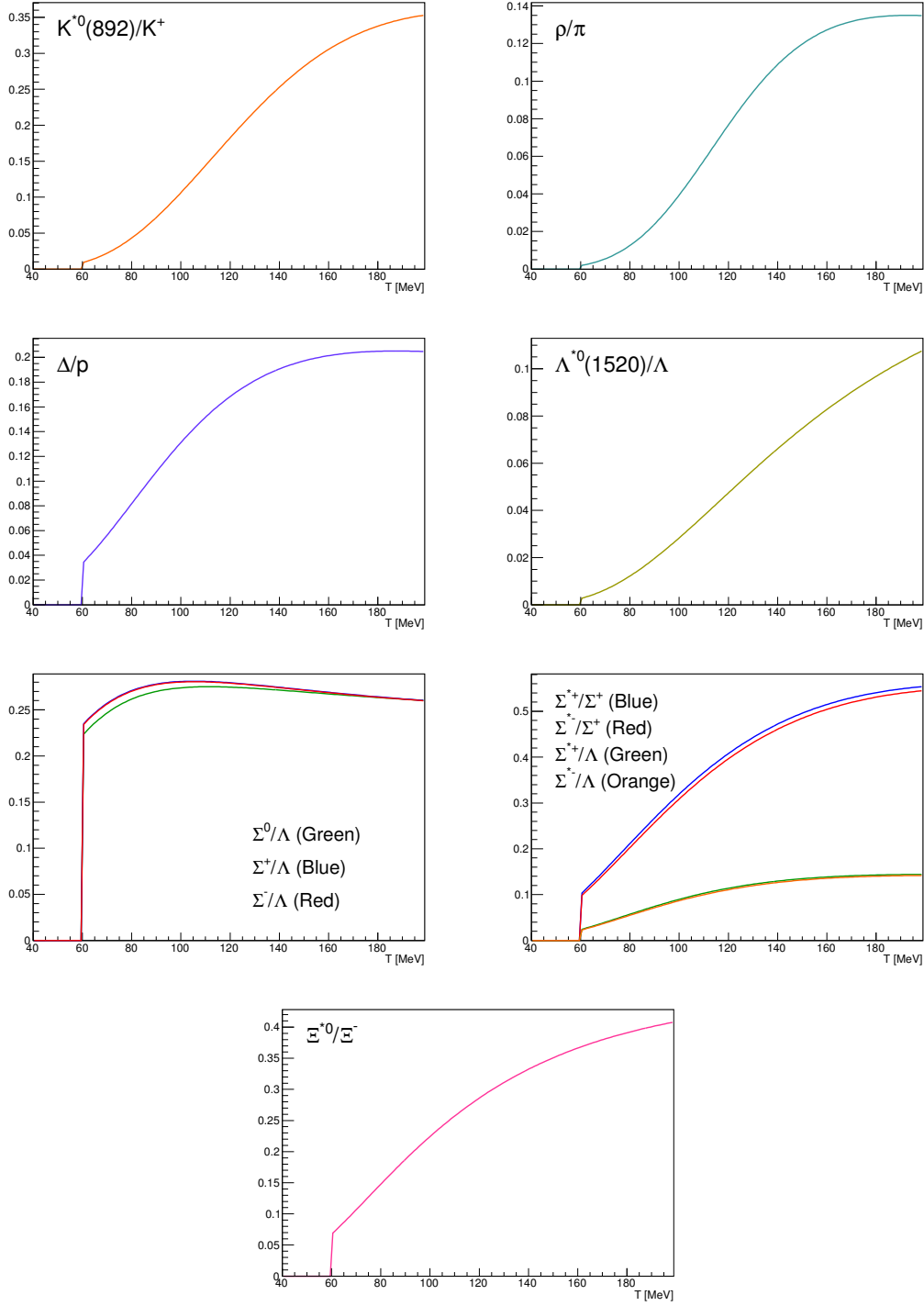


Figure 1: Ratio of baryonic and mesonic resonances over their stable partner as a function of temperature.

Table 3: Difference of mass (ΔM), baryon number (ΔB), strangeness (ΔS) and charge (ΔQ) of the ratios. The values of the slopes needs to be checked!!!!

Particle	Δ^{++}/p	K^*/K^+	Λ^*/Λ	Σ^{*+}/Λ	Σ^{*+}/Σ^0	Σ^0/Λ	Σ^{*+}/Σ^+	Ξ^{*0}/Ξ^-
ΔM (MeV/ c^2)	293.8	402.25	403.82	267.12	190.16	76.96	193.43	210.49
ΔB	0	0	0	0	0	0	0	0
ΔS	0	0	0	0	0	0	0	0
ΔQ	+1	-1	0	+1	0	+1	0	-1
Slope (%) per MeV ????????	0.19	0.76	0.98	0.25	-	-0.08	0.37	0.42

235 3.1.3 Comparison with data

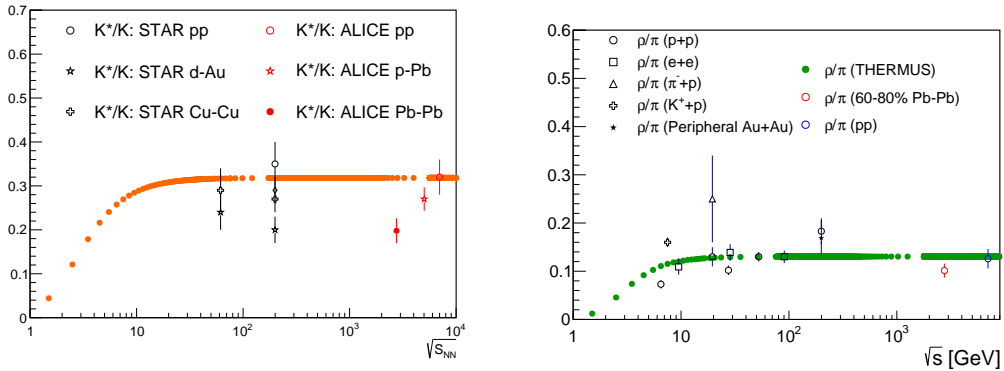


Figure 2: Ratio of resonances over their stable partner as a function of $\sqrt{(s)}$.

236 3.2 UrQMD

237 4 A Large Ion Collider Experiment at the LHC

238 ALICE (A Large Ion Collider Experiment) has been collecting data during the whole first
 239 phase of the Large Hadron Collider operations, from its startup on the 23 November 2009
 240 to the beginning of the first long technical shutdown in February 2013. During the first
 241 three years of operations LHC provided pp collisions at 0.9, 2.76, 7 and 8 TeV, Pb?Pb
 242 collisions at 2.76A TeV and finally p?Pb collisions at 5.02 TeV. The first section of this
 243 chapter focuses on the LHC performance during this phase and includes details on the
 244 accelerator parameters that allow the LHC to perform as a lead ion collider. A detailed
 245 description of the ALICE detector follows in the section 2.2. ALICE has been designed and

246 optimized to study the high particle-multiplicity environment of ultra-relativistic heavy-ion
247 collisions and its tracking and particle identification performance in Pb-Pb collisions are
248 discussed. The attention is drawn in particular on the central barrel detectors. Section
249 2.3 de- scribes the ALICE Data Acquisition (DAQ) system, that also embeds tools for the
250 online Data Quality Monitoring (DQM). The final part of the chapter is dedicated to the
251 offline computing and reconstruction system based on the GRID framework.

252 **4.1 The Large Hadron Collider**

253 The Large Hadron Collider (LHC) [12] is a two-ring-superconducting hadron accelerator
254 and collider installed in the 26.7 Km tunnel that hosted the LEP machine and it completes
255 the CERN accelerator complex together with the PS and SPS, among the others shown
256 in fig. 2.1. Four main experiments are located in four different interaction points along
257 its circumference. ATLAS and CMS, the biggest ones, are multi-purpose detectors built
258 to discover the Higgs boson and hints of new physics beyond the Standard Model. LHCb
259 is dedicated to the physics of the flavour, focusing on the study CP-violation using B
260 meson decay channels. The phenomena that these three experiments aim to observe have
261 production cross sec- tion of the order of a hundred of pb or lower, therefore a large number
262 of collision events is required to the machine in order to fulfill the LHC pp physics program.
263 ALICE, on the contrary, is dedicated to the physics of Quark Gluon Plasma through the
264 observation of high-energy heavy-ion collisions, although a shorter physics pro- gram with
265 pp collisions has been carried out.

266 **4.2 The ALICE project**

267 **4.2.1 ALICE detector**

268 **4.2.2 Data Acquisition (DAQ) and trigger system**

269 **4.2.3 ALICE offline software frame work**

270 **5 Measurement of $\Xi(1530)^0$ production in p–Pb and Pb–Pb**

271 The measurement of resonance production in p–Pb collisions helps to disentangle cold
272 nuclear matter effects from genuine hot medium effects and contribute to the study of
273 the system size dependence of re-scattering in the hadronic phase. And the measurement
274 in ultra-relativistic heavy-ion collisions such as Pb–Pb collisions, provide information on
275 the properties of hadronic medium and different stage of its evolution. In order to study
276 the particle production mechanism in the hadronic phase between the chemical and ki-
277 netic freeze-out, the $\Xi(1530)^0$ resonance production at mid-rapidity($-0.5 < y_{\text{CMS}} < 0$) is
278 measured in p–Pb collisions $\sqrt{s_{\text{NN}}} = 5.02$ TeV and in Pb–Pb collisions with $|y| < 0.5$ at
279 $\sqrt{s_{\text{NN}}} = 2.76$ TeV with the ALICE experiment, via the reconstruction of its hadronic decay
280 into $\Xi\pi$.

281 **5.1 $\Xi(1530)^0$ -reconstruction**

282 The Ξ^{*0} production in p–Pb and Pb–Pb collisions at mid-rapidity has been studied in dif-
283 ferent multiplicity classes, from very central to peripheral collisions. The analysis strategy
284 is based on the invariant mass study of the reconstructed pairs (referred to as the candi-
285 dates) whose provenance could be the decay of a Ξ^{*0} baryon into charged particles. The
286 decay products (also called daughters in the text) are identified as oppositely charged Ξ and
287 π among the tracks reconstructed in the central barrel. The event selection, track selec-
288 tion and the particle identification strategy is described. The raw signal yield is extracted
289 by fitting the background-subtracted invariant mass distribution in several transverse mo-
290 mentum intervals. In order to extract the p_T -dependent cross section, these yields are
291 corrected for efficiency. The p_T -dependent correction due to the detector acceptance and
292 reconstruction efficiency, $(\text{Acc} \times \epsilon_{rec})(p_T)$, is computed from a Monte Carlo simulation.
293 The absolute normalisation is then performed, by dividing for the number of the events in
294 each multiplicity and centrality classes.

295 **5.1.1 Data sample and event selection**

296 A description of the ALICE detector and of its performance during the LHC Run 1 (2010–
297 2013) can be found in [13, 14]. The data sample in the analysis from Pb–Pb collisions with
298 energy of $\sqrt{s_{\text{NN}}} = 2.76$ obtained during 2011 and the sample of p–Pb run at $\sqrt{s_{\text{NN}}} = 5.02$
299 TeV was recorded in 2013.

300 Due to the asymmetric energies of the proton (4 TeV) and lead ion (1.57 A TeV) beams,
301 the centre-of-mass system in the nucleon-nucleon frame is shifted in rapidity by $\Delta y_{\text{NN}} =$
302 0.465 towards the direction of the proton beam with respect to the laboratory frame of
303 the ALICE detector [2]. For the analysed p–Pb data set, the direction of the proton beam
304 was towards the ALICE muon spectrometer, the so-called “C” side, standing for negative
305 rapidities; conversely, the Pb beam circulated towards positive rapidities, labelled as “A”
306 side in the following. The analysis in this paper was carried out at midrapidity, in the
307 rapidity window $-0.5 < y_{\text{CMS}} < 0$.

308 The minimum-bias trigger during the p–Pb run was configured to select events by
309 requiring a logical OR of signals in V0A and V0C [14], two arrays of 32 scintillator detectors
310 covering the full azimuthal angle in the pseudo-rapidity regions $2.8 < \eta_{\text{lab}} < 5.1$ and
311 $-3.7 < \eta_{\text{lab}} < -1.7$, respectively [15]. In the data analysis it was required to have a
312 coincidence of signals in both V0A and V0C in order to reduce the contamination from
313 single-diffractive and electromagnetic interactions. Out of this sample in p–Pb collision
314 events about 109.3 million events, 93.9 million events satisfy the following selection criteria
315 and have been actually used for the analysis.

316 The Pb–Pb collisions data sample was selected by online centrality trigger requiring a
317 signal in the forward V0 detectors[16] to record enhanced data in central collision. The
318 data consists of 24.8 million events in most central collisions (0-10%), 21.8 million events in
319 semi-central collisions (10-50%) and 3.5 million events with minimum-bas trigger (0-90%).

320 Among 49.6 million events in total, 43.0 million events have been analyzed as passed the
 321 criteria below.

- 322 • Events with z-coordinate of primary vertex (V_z) falling within ± 10 cm from the
 323 interaction point
- 324 • Rejection of pile-up event
- 325 • Requiring primary tracks to have at least one hit in one of the two innermost layers
 326 of the ITS (silicon pixel detector, SPD)
- 327 • p–Pb: multiplicity ranges in percentile (V0A): 0-20%, 20-40%, 40-60%, 60-100% and
 328 MB(0-100%)
- 329 • Pb–Pb: centrality classes (V0A and V0C): 0-10%, 10-40%, 40-80% and MB (0-80%)

330 The distribution of the vertex z position of the accepted events in p–Pb collision is
 331 reported on left panel in Figure 3 and corresponding figure but obtained from Pb–Pb
 332 collisions is shown on right panel in Figure. 3. Events with $|V_z| < 10$ cm have been used
 333 to ensure a uniform acceptance in the central pseudo-rapidity region, $|\eta| < 0.8$, where the
 334 analysis is performed. This cut reduces the total number of events to 97.5 million events,
 335 that is the $\sim 89.2\%$ of the initial sample in p–Pb collisions and 43.04 million events which
 336 is $\sim 86.8\%$ of the initial sample in Pb–Pb collisions are survived.

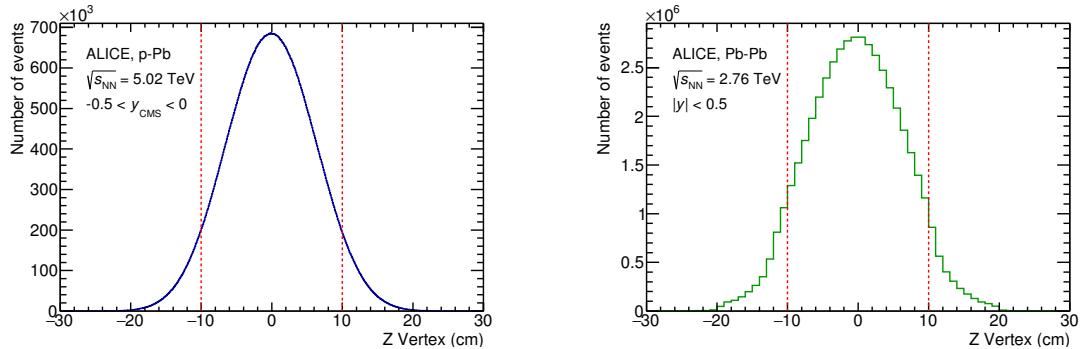


Figure 3: Vertex-z coordinate distribution of the accepted events in p–Pb collision(Left) and in Pb–Pb collisions(Right). The red dashed line indicates vertex cut

337 Fig. 4 shows the multiplicity distribution of the accepted events in p–Pb collision
 338 divided in bins of percentile. The each color on the histogram indicate the multiplicity
 339 ranges used in this analysis. Corresponding events for each multiplicity range are in Table
 340 4.

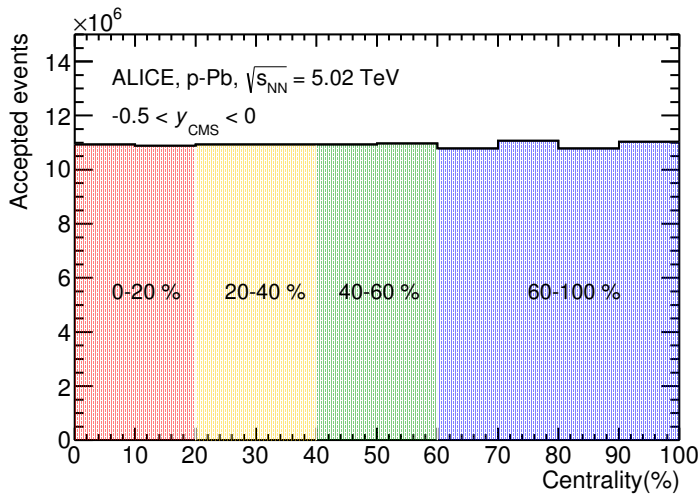


Figure 4: Multiplicity distribution of accepted events in p–Pb collision in percentile. The each color and labels define the four intervals in which the analysis is performed.

341 The distribution of centrality in each trigger used to select the events in Pb–Pb collision
 342 is shown in Fig. 5 and the reason why the centrality has step structure is that there are
 343 three different trigger classes classified by the amplitude threshold on VZERO detector.
 344 Because the distribution of events as function of centrality is not a flat, this may lead to
 345 additional bias, in particular when one needs to combine the results from different triggers.
 346 For example, events from 40-80% centrality bin have bias with high statistics in 40-60%. In
 347 order to avoid this effect, we have applied a flattening procedure to have flat distribution
 348 of events as function of centrality. A brief explanation of the method is below :

- 349 1. Histograms are obtained for the effective mass distribution in 1% centrality bins and
 350 for the centrality distribution
- 351 2. The effective mass distributions are scaled in each 1% centrality bin by a factor:
 352 Factor = Nevent in 20-40% / 20 / Nevent in current 1% bin
- 353 3. Each bin in the centrality distribution is scaled using the factor described above
- 354 4. Histograms are added for centrality bins of interest: 0-10%, 10-40%, 40-80%, 0-80%

355 The resulting number of events in each centrality classes is summarized in Table 4.

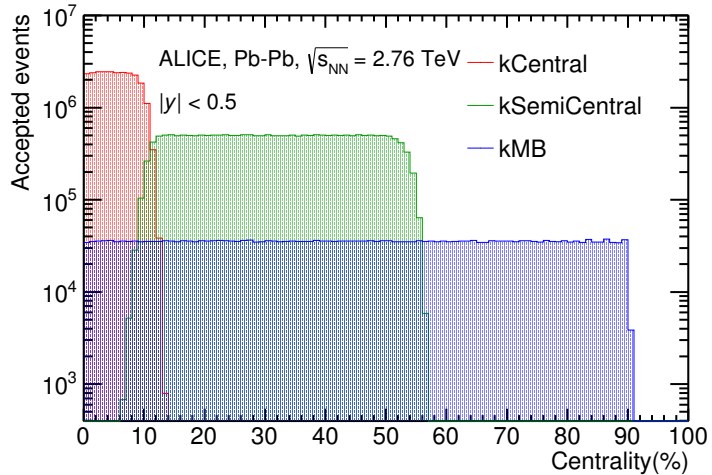


Figure 5: Centrality distribution of three different trigger classes.

p-Pb	0-20%	21.82×10^6
	20-40%	21.86×10^6
	40-60%	21.91×10^6
	60-100%	43.68×10^6
Pb-Pb	0-10%	5.58×10^6
	10-40%	16.73×10^6
	40-80%	22.31×10^6

Table 4: Number of accepted and analyzed events per multiplicity/centrality interval

356 5.1.2 Track and topological selection

357 In comparison with the Ξ^{*0} analysis carried out in pp collisions at $\sqrt{s} = 7$ TeV [4], track
 358 and topological selections were revised and adapted to the p-Pb dataset. Pions from strong
 359 decays of Ξ^{*0} were selected according to the criteria for primary tracks. As summarized
 360 in Table 5, all charged tracks were selected with $p_T > 0.15$ GeV/c and $|\eta_{\text{lab}}| < 0.8$,
 361 as described in Ref. [14]. The primary tracks were chosen with the Distance of Closest
 362 Approach (DCA) to PV of less than 2 cm along the longitudinal direction (DCA_z) and
 363 lower than $7\sigma_r$ in the transverse plane (DCA_r), where σ_r is the resolution of DCA_r . The σ_r
 364 is strongly p_T -dependent and lower than 100 μm for $p_T > 0.5$ GeV/c [14]. To ensure a good
 365 track reconstruction quality, candidate tracks were required to have at least one hit in one
 366 of the two innermost layers (SPD) of the ITS and to have at least 70 reconstructed points in

³⁶⁷ the Time Projection Chamber (TPC), out of a maximum of 159. The Particle IDentification
³⁶⁸ (PID) criteria for all decay daughters are based on the requirement that the specific energy
³⁶⁹ loss (dE/dx) is measured in the TPC within three standard deviations (σ_{TPC}) from the
expected value (dE/dx_{exp}), computed using a Bethe-Bloch parametrization [14].

Common track selections	$ \eta_{\text{lab}} $	< 0.8
	p_T	$> 0.15 \text{ GeV}/c$
	PID $ (\text{d}E/\text{d}x) - (\text{d}E/\text{d}x)_{\text{exp}} $	$< 3 \sigma_{\text{TPC}}$
Primary track selections	DCA_z to PV	$< 2 \text{ cm}$
	DCA_r to PV	$< 7\sigma_r - 10\sigma_r (p_T)$
	number of SPD points	≥ 1
	number of TPC points	> 70
	χ^2 per cluster	< 4

Table 5: Track selections common to all decay daughters and primary track selections applied to the charged pions from decays of Ξ^{*0} .

³⁷⁰ Since pions and protons from weak decay of Λ ($c\tau = 7.89 \text{ cm}$ [17]) and pions from weak
³⁷¹ decay of Ξ^- ($c\tau = 4.91 \text{ cm}$ [17]) are produced away from the PV, specific topological and
³⁷³ track selection criteria, as summarized in Table 6, were applied [3, 4, 18].

Topological cuts	p–Pb	Pb–Pb
DCA_r of Λ decay products to PV	$> 0.06 \text{ cm}$	$> 0.11 \text{ cm}$
DCA between Λ decay products	$< 1.4 \text{ cm}$	$< 0.95 \text{ cm}$
DCA of Λ to PV	$> 0.015 \text{ cm}$	> 0.06
$\cos\theta_\Lambda$	> 0.875	> 0.998
$r(\Lambda)$	$0.2 < r(\Lambda) < 100 \text{ cm}$	$0.2 < r(\Lambda) < 100 \text{ cm}$
$ M_{p\pi} - m_\Lambda $	$< 7 \text{ MeV}/c^2$	$< 7 \text{ MeV}/c^2$
DCA_r of pion (from Ξ^-) to PV	$> 0.015 \text{ cm}$	$> 0.035 \text{ cm}$
DCA between Ξ^- decay products	$< 1.9 \text{ cm}$	< 0.275
$\cos\theta_\Xi$	> 0.981	> 0.9992
$r(\Xi^-)$	$0.2 < r(\Xi^-) < 100 \text{ cm}$	$0.2 < r(\Xi^-) < 100 \text{ cm}$
$ M_{\Lambda\pi} - m_\Xi $	$< 7 \text{ MeV}/c^2$	$< 7 \text{ MeV}/c^2$

Table 6: Topological and track selection criteria.

³⁷⁴ In the analysis of Ξ^{*0} , Λ and π from Ξ^- were selected with a DCA of less than 1.9 cm
³⁷⁵ and with a DCA_r to the PV greater than 0.015 cm. The Λ daughter particles (π and p)
³⁷⁶ were required to have a DCA_r to the PV greater than 0.06 cm, while the DCA between the
³⁷⁷ two particles was required to be less than 1.4 cm. Cuts on the invariant mass, the cosine

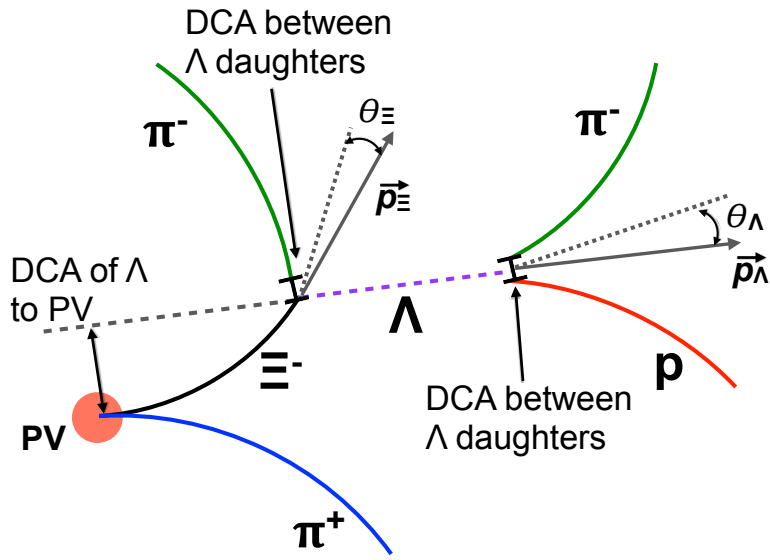


Figure 6: Sketch of the decay modes for Ξ^{*0} and depiction of the track and topological selection criteria.

³⁷⁸ of the pointing angle ($\theta_\Lambda, \theta_\Xi$) and the radius of the fiducial volume ($r(\Lambda), r(\Xi)$) in Table 6
³⁷⁹ were applied to optimize the balance of purity and efficiency of each particle sample.

380 **5.1.3 Particle identification**

381 PID selection criteria are applied for

- 382 1. π^\pm (last emitted π) and proton from Λ
383 2. π^\pm (second emitted π) from Ξ^\pm
384 3. π^\pm (first emitted π) from $\Xi(1530)^0$

385 by using TPC. On TPC dE/dx versus momentum distribution, 3σ cuts are applied to TPC
386 for selecting each of the particles. The TPC dE/dx selection allows to have better signal
387 with $\sim 20\%$ increase of significance.

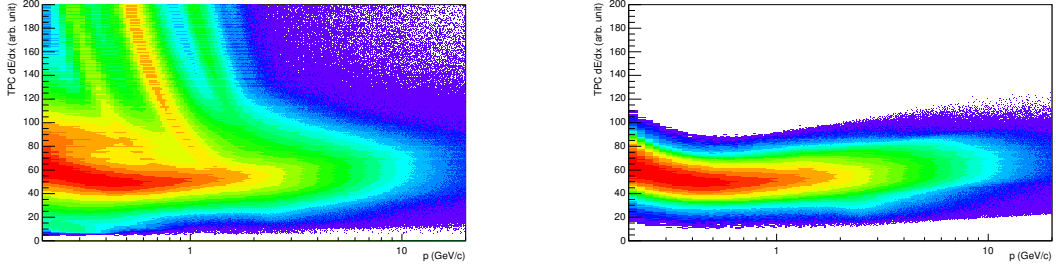


Figure 7: TPC dE/dx as function of transverse momentum for total (top) and selected first emitted π in 3σ (bottom)

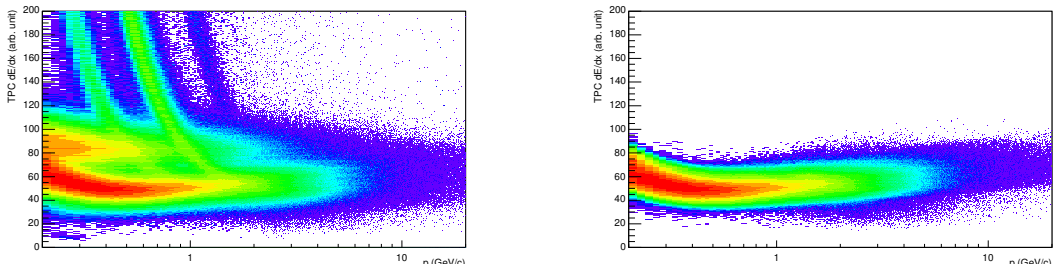


Figure 8: TPC dE/dx as function of transverse momentum for total (top) and selected second emitted π in 3σ (bottom)

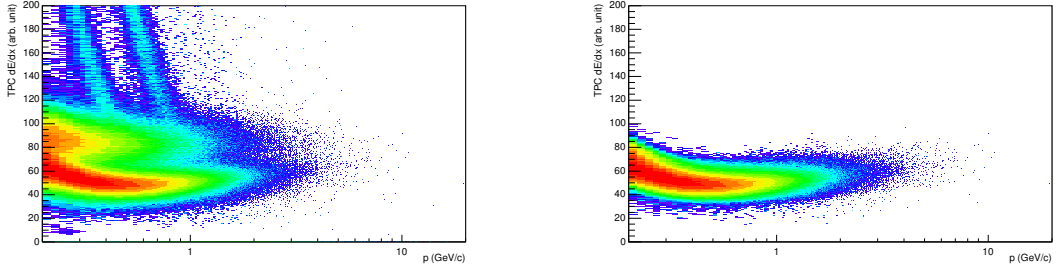


Figure 9: TPC dE/dx as function of transverse momentum for total (top) and selected last emitted π in 3σ (bottom)

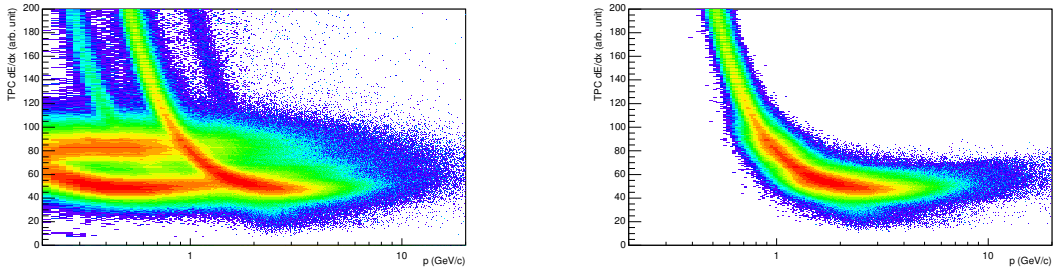


Figure 10: TPC dE/dx as function of transverse momentum for total (top) and selected proton in 3σ (bottom)

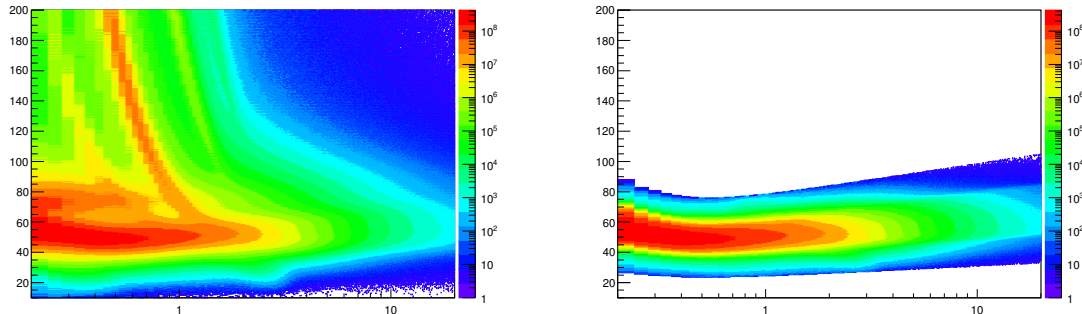


Figure 11: TPC dE/dx as function of transverse momentum for total (top) and selected first emitted π in 3σ (bottom)

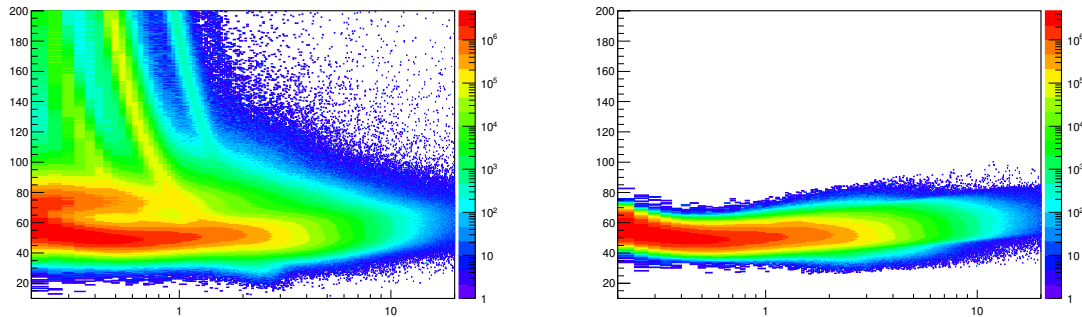


Figure 12: TPC dE/dx as function of transverse momentum for total (top) and selected second emitted π in 3σ (bottom)

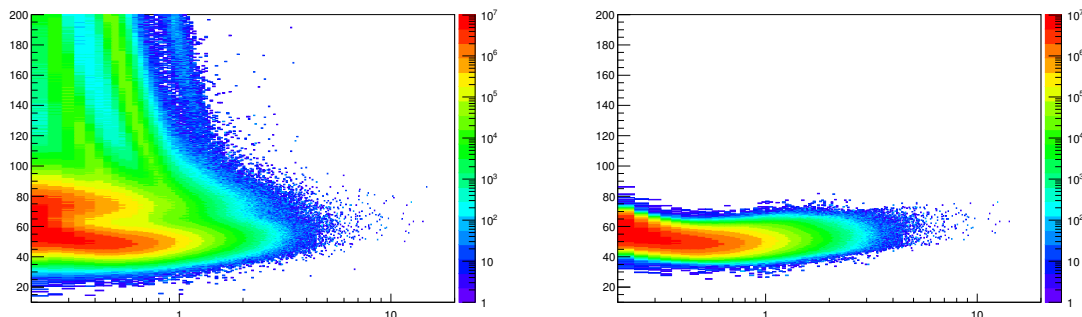


Figure 13: TPC dE/dx as function of transverse momentum for total (top) and selected last emitted π in 3σ (bottom)

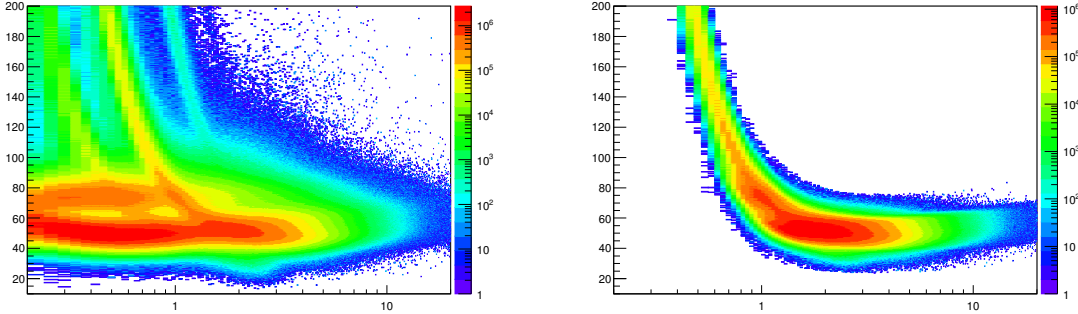


Figure 14: TPC dE/dx as function of transverse momentum for total (top) and selected proton in 3σ (bottom)

388 5.1.4 Signal extraction

389 The Ξ^{*0} signals were reconstructed by invariant-mass analysis of candidates for the decay
 390 products in each transverse momentum interval of the resonance particle, and for each
 391 multiplicity class. The $\Xi^-\pi^+(\Xi^+\pi^-)$ invariant mass distribution is reported in Figure 5.1.4
 392 for semi-central events (20-40%) in p-Pb collisions and Figure 5.1.4 for central events(0-
 393 10%) in Pb-Pb collisions.

394 Since the resonance decay products originate from a position which is indistinguishable
 395 from the PV, a significant combinatorial background is present. In order to extract
 396 $\Xi(1530)^0$ signal it is necessary to remove or, at least reduce, the combinatorial background.
 397 For this analysis, this has been done with the event mixing (EM) technique, by combining
 398 uncorrelated decay products 20 different events in p-Pb (5 different events in Pb-Pb). The
 399 events for the mixing have been selected by applying the similarity criteria to minimise
 400 distortions due to different acceptances and to ensure a similar event structure, only tracks
 401 from events with similar vertex positions z ($|\Delta z| < 1$ cm) and track multiplicities n ($|\Delta n| <$
 402 10) were taken.

403 The mixed-event background distributions were normalised to two fixed regions,
 404 $1.49 < M_{\Xi\pi} < 1.51 \text{ GeV}/c^2$ and $1.56 < M_{\Xi\pi} < 1.58 \text{ GeV}/c^2$, around the Ξ^{*0} mass
 405 peak (Figure 5.1.4 and 5.1.4). These regions were used for all p_T intervals and multiplicity
 406 classes, because the background shape is reasonably well reproduced in these regions and
 407 the invariant-mass resolution of the reconstructed peaks appears stable, independently of
 408 p_T . The uncertainty on the normalisation was estimated by varying the normalisation
 409 regions and is included in the quoted systematic uncertainty for the signal extraction (Sec-
 410 tion 5.4).

411 After the background subtraction, the resulting distribution is shown in Figure 5.1.4
 412 and 5.1.4. In order to obtain raw yields, a combined fit of a first-order polynomial for

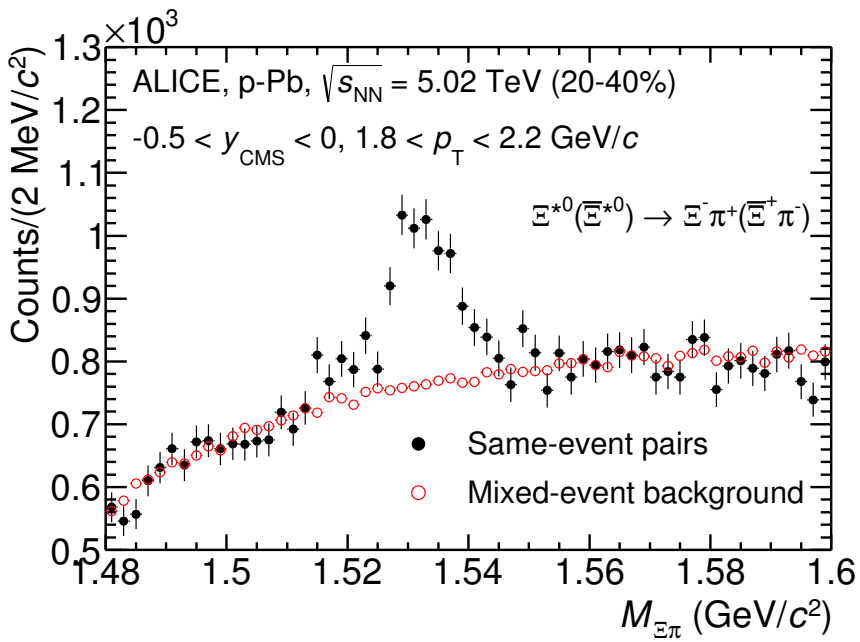


Figure 15: The $\Xi^\pm\pi^\pm$ invariant mass distribution (Same-event pairs) in $1.8 < p_T < 2.2 \text{ GeV}/c$ and for the multiplicity class 20-40%. The background shape, using pairs from different events (Mixed-event background), is normalised to the counts in $1.49 < M_{\Xi\pi} < 1.51 \text{ GeV}/c^2$ and $1.56 < M_{\Xi\pi} < 1.58 \text{ GeV}/c^2$.

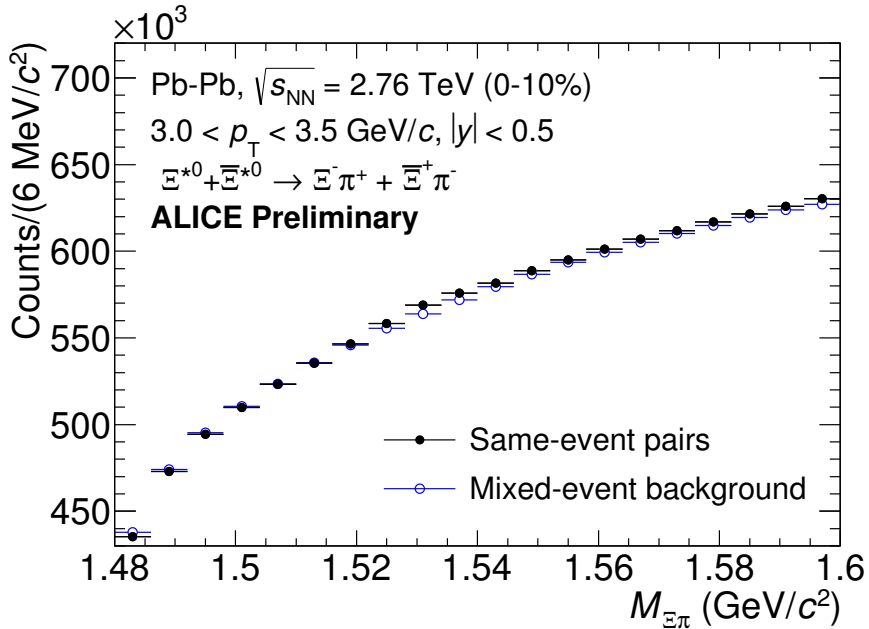


Figure 16: The $\Xi^\pm \pi^\pm$ invariant mass distribution (Same-event pairs) in $3.0 < p_T < 3.5 \text{ GeV}/c$ and for the centrality class 0-10%. The background shape, using pairs from different events (Mixed-event background), is normalised to the counts in $1.49 < M_{\Xi\pi} < 1.51 \text{ GeV}/c^2$ and $1.56 < M_{\Xi\pi} < 1.58 \text{ GeV}/c^2$.

⁴¹³ the residual background and a Voigtian function (a convolution of a Breit-Wigner and a
⁴¹⁴ Gaussian function accounting for the detector resolution) for the signal was used. The
⁴¹⁵ mathematical form of fit function used in analysis is:

$$f(M_{\Xi\pi}) = \frac{Y}{2\pi} \frac{\Gamma_0}{(M_{\Xi\pi} - M_0)^2 + \frac{\Gamma_0^2}{4}} \frac{e^{-(M_{\Xi\pi} - M_0)/2\sigma^2}}{\sigma\sqrt{2\pi}} + bg(M_{\Xi\pi}) \quad (1)$$

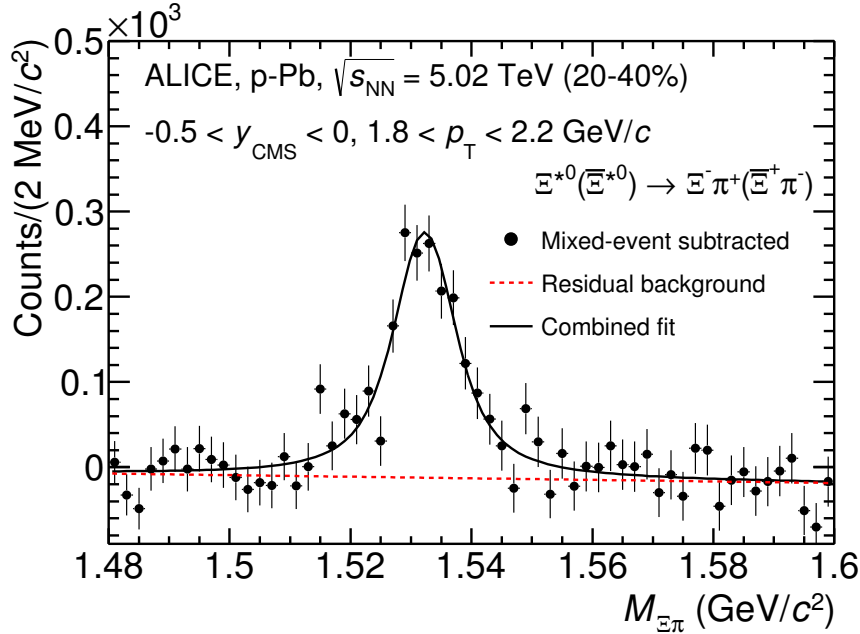


Figure 17: The invariant mass distribution after subtraction of the mixed-event background in p–Pb collisions. The solid curve represents the combined fit, while the dashed line describes the residual background.

⁴¹⁶ The mass parameter of the Voigtian fit (M_0) is left free within the fit range ($1.48 \text{ GeV}/c^2$
⁴¹⁷ and $1.59 \text{ GeV}/c^2$). The overall invariant mass width of the Voigtian function is governed
⁴¹⁸ by 2 parameters: σ and Γ_0 . The σ describes the broadening of the peak due to finite
⁴¹⁹ detector resolution while Γ describes the intrinsic width of the resonance itself. The Γ_0 is
⁴²⁰ fixed to the PDG value of $9.1 \text{ MeV}/c$ for the $\Xi(1530)^0$. Because of lack of statistics, the
⁴²¹ σ can be over estimated. Therefore the σ parameter is fixed to value derived from σ in
⁴²² MB events which has largest statistics. The σ as function of p_T distribution in MB events
⁴²³ is shown in Figure. 19 and we also report invariant mass of $\Xi(1530)^0$ as function of p_T in
⁴²⁴ Figure. 20. The $\Xi(1530)^0$ raw yields have been extracted from the fit for the 4 multiplicity

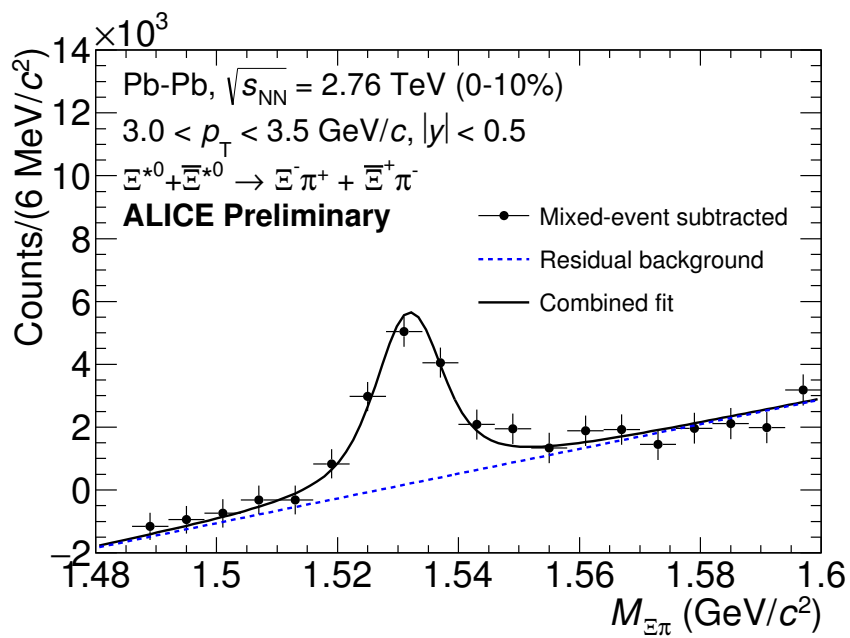


Figure 18: The invariant mass distribution after subtraction of the mixed-event background in Pb–Pb collisions. The solid curve represents the combined fit, while the dashed line describes the residual background.

⁴²⁵ bins (+ NSD events) in p–Pb and 4 centrality bins in Pb–Pb collisions and the yields as
⁴²⁶ function of p_T are shown in Figure 21.

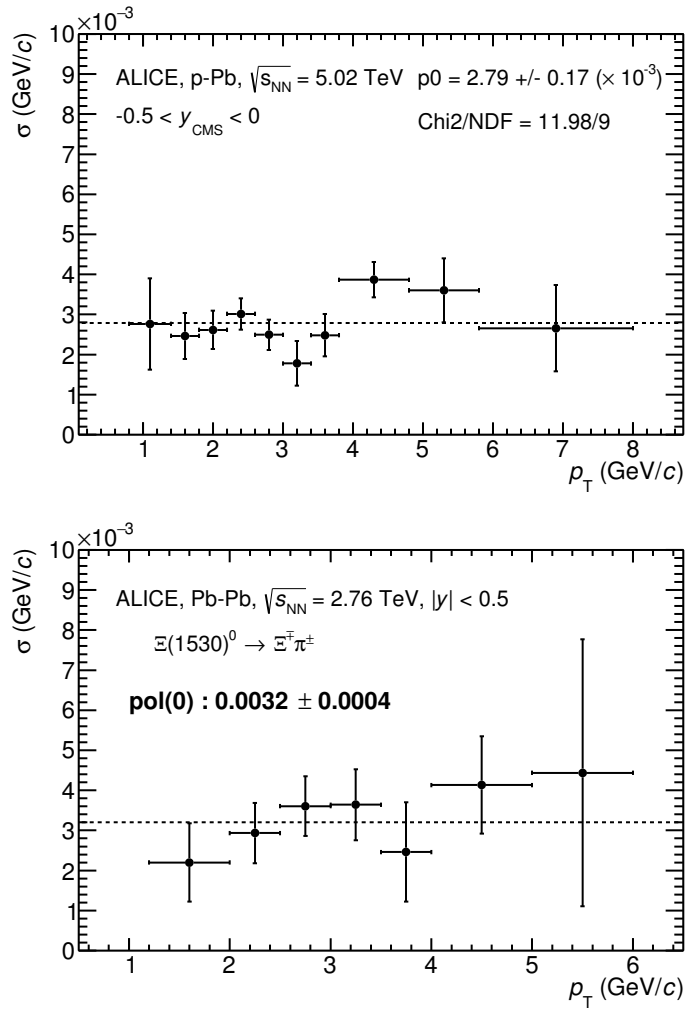


Figure 19: σ fit parameters as a function of p_T in MB in p–Pb collisions (top) and in Pb–Pb collisions (bottom).

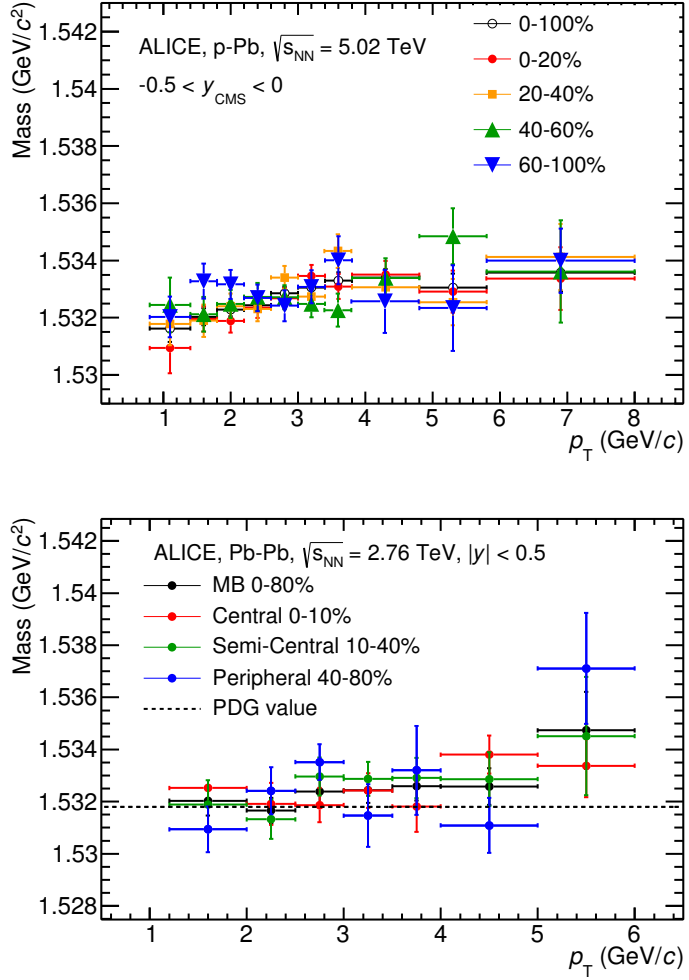


Figure 20: $\Xi(1530)^0$ -mass obtained from fit of the Voigtian peak as a function of p_T in each multiplicity classes in p-Pb collisions (top) and the different centrality classes in Pb-Pb (bottom).

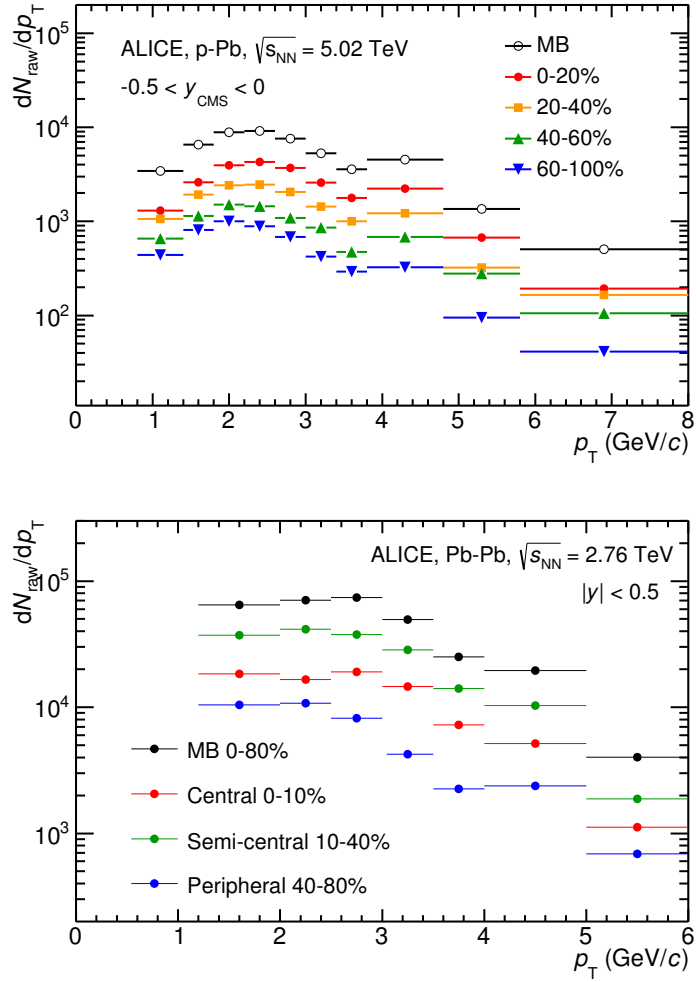


Figure 21: $\Xi(1530)^0$ -raw spectra obtained from fit of the Voigtian peak and a polynomial residual background for different multiplicities in p-Pb collisions (top) and Pb-Pb collisions (bottom). Only the statistical error is reported.

427 **5.2 Efficiency correction**

428 The raw yields were corrected for the geometrical acceptance and the reconstruction effi-
 429 ciency ($A \times \epsilon$) of the detector (Figure. 22). By using the DPMJET 3.05 event generator [19]
 430 and the GEANT 3.21 package [20], a sample of about 100 million p–Pb events was sim-
 431 ulated and reconstructed in order to compute the corrections. The distributions of $A \times \epsilon$
 432 were obtained from the ratio between the number of reconstructed Ξ^{*0} and the number of
 433 generated particle in the same p_T and rapidity interval. Since the correction factors for
 434 different multiplicity classes are in agreement with those from MB events within statistical
 435 uncertainty, the latter were used for all multiplicity classes.

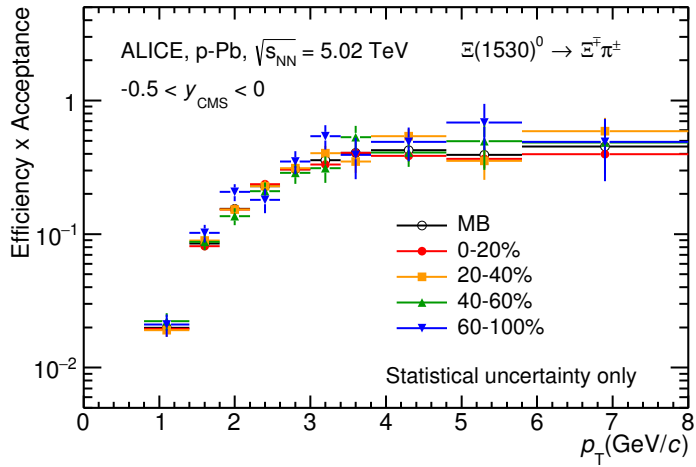


Figure 22: $\Xi(1530)^0$ -raw spectra obtained from fit of the Voigtian peak and a polynomial residual background for different multiplicities. Only the statistical error is reported.

436 Because the generated $\Xi(1530)^0$ spectra have different shapes than the measured $\Xi(1530)^0$
 437 spectra, it is necessary to weight the generated and reconstructed $\Xi(1530)^0$ spectra in these
 438 simulations. Fig. 23 shows the generated and reconstructed $\Xi(1530)^0$ spectra plotted with
 439 the (corrected) measured $\Xi(1530)^0$ spectrum for MB events and the Levy fit of that mea-
 440 sured spectrum. The generated and measured $\Xi(1530)^0$ spectra have different behaviours
 441 for the range $0.5 < p_T < 1$ GeV/ c . The generated $\Xi(1530)^0$ spectrum decreases with
 442 increasing p_T over this range, while the fit of the measured $\Xi(1530)^0$ spectrum reaches a
 443 local maximum in this range. The correction ϵ is observed to change rapidly over this
 444 p_T range. It is therefore necessary to weight the generated spectrum so that it has the
 445 shape of the measured $\Xi(1530)^0$ spectrum (and to apply corresponding weights to the re-
 446 constructed $\Xi(1530)^0$ spectrum). An iterative procedure is performed to determine the
 447 correct weighting (and therefore the correct ϵ).

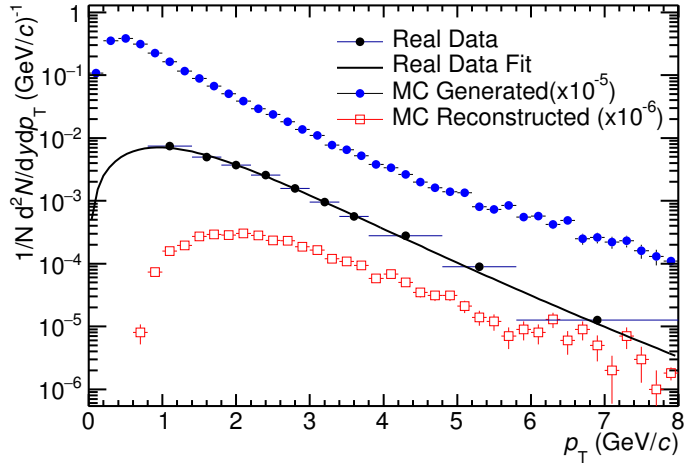


Figure 23: Real corrected $\Xi(1530)^0$ spectrum (black) for the minimum bias with Levy fit (black curve). Also shown are the unweighted generated (blue) and reconstructed (red) $\Xi(1530)^0$ spectra.

- 448 1. The unweighted ϵ is calculated.
- 449 2. This ϵ is used to correct the measured xis spectrum.
- 450 3. The corrected $\Xi(1530)^0$ spectrum is fit.
- 451 4. This fit is used to weight the simulated xis spectra. A p_T dependent weight is applied
452 to the generated xis spectrum so that it follows the fit. The same weight is applied
453 to the reconstructed xis spectrum.
- 454 5. The (weighted) ϵ is calculated.
- 455 6. Steps 2-5 are repeated (with the weighted ϵ from step 5 used as the input for step 2)
456 until the ϵ values are observed to change by $< 0.1\%$ (relative) between iterations. It
457 is observed that four iterations are sufficient for this procedure to converge.

458 Finally, the re-weighted efficiency is obtained and the distribution as function of p_T is
459 shown in Figure 24.

460 In order to obtain the correction factor dedicated in Pb-Pb collisions, MC events are
461 generated using Heavy Ion Jet Interaction Generator (HIJING). The generated events are
462 passed through a GEANT3 model of the ALICE experiment with a realistic description of
463 the detector response. Because we have observed centrality dependent efficiency, the cen-
464 trality dependent efficiencies have been applied to get corrected raw yield. The reweighting

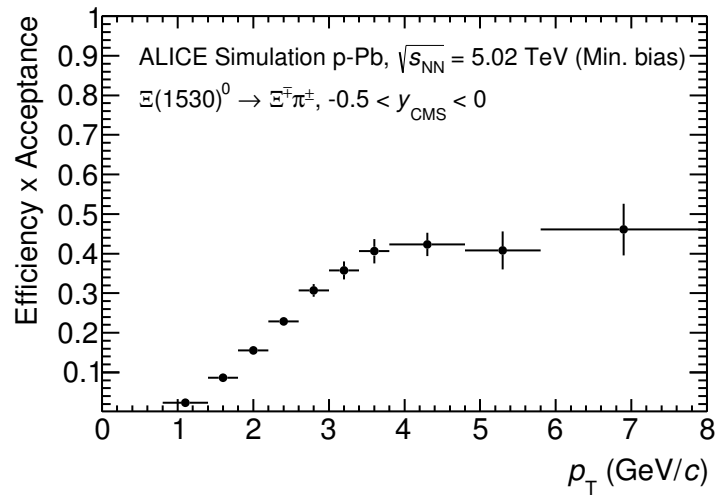


Figure 24: Efficiency as a function of p_T in minimum bias events in p–Pb collisions.

465 approach which was used to correct the efficiency in p–Pb is also applied to the efficiency
 466 obtained in Pb–Pb.

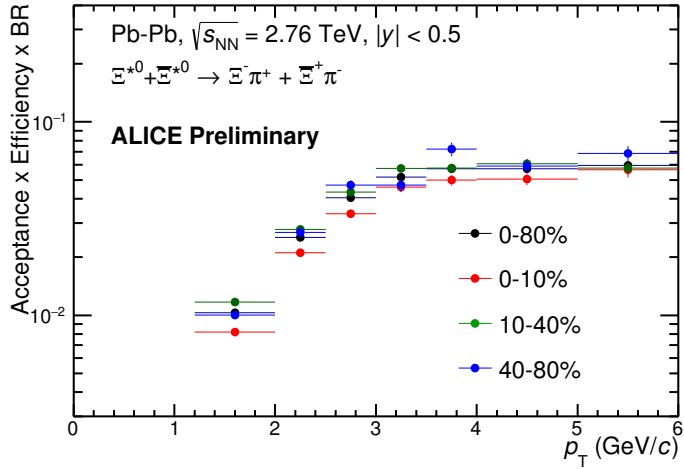


Figure 25: Efficiency as a function of p_T in different centrality classes in Pb–Pb collisions

467 5.3 Corrected p_T -spectra

468 The p_T spectrum is by the number of produced particles of a given type in the desired
 469 interval of phase-space divided by the number of inelastic collisions. The spectrum is
 470 calculated as:

$$\frac{1}{N} \times \frac{d^2N}{dydp_T} = \frac{1}{N_{E,PhysSel}} \times \frac{N_{raw}}{dp_T dy} \frac{1}{\epsilon} \frac{N_{total}^{MC}}{N_{post-PVcut}^{MC}}, \quad (2)$$

471 where N_E represent the number inelastic collisions, the $\frac{dN}{dydp_T}$ is the yield per range of
 472 rapidity y , per range in p_T . On the right hand side $N_{E,PhysSel}$ is the number of events
 473 counted by the physics selection trigger. N_{raw} is the raw extracted number of particle in the
 474 rapidity and p_T bin of width $\Delta y = 0.5$ in p–Pb ($\Delta y = 1.0$ in Pb–Pb) and Δp_T , respectively.
 475 ϵ is the reconstruction efficiency estimated from Monte Carlo simulations. $\frac{N_{total}^{MC}}{N_{post-PVcut}^{MC}}$ is the
 476 ratio of the total number of particle from MC divided by the number of particle from MC
 477 after the Primary-Vertex cut is imposed. It takes into account the fraction of particle lost
 478 after imposing the PV cut. We notice that for minimum-bias results in p–Pb, we adopted
 479 a normalisation such that to provide result from non-single diffractive(NSD) cross-section.
 480 The normalisation factor is 0.964 [2]. The obtained spectrum at MB and the spectrums
 481 from different multiplicity classes in p–Pb are shown in Figure 26 and different centrality
 482 classes in Pb–Pb are shown in Figure 27.

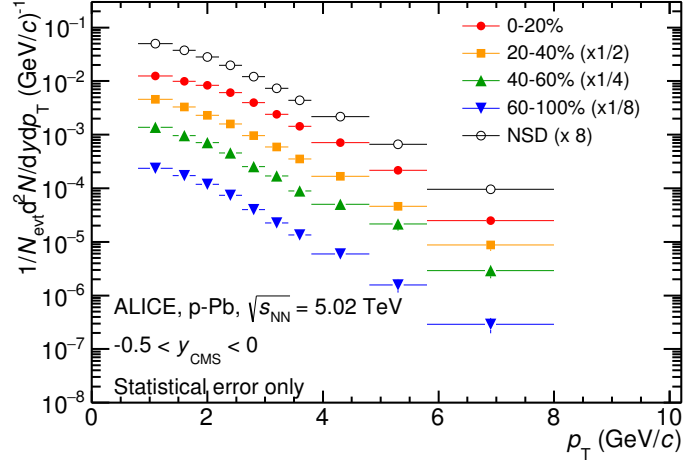


Figure 26: Corrected p_T -spectra of $\Xi(1530)^0$ in NSD and different multiplicity classes in p-Pb collisions.

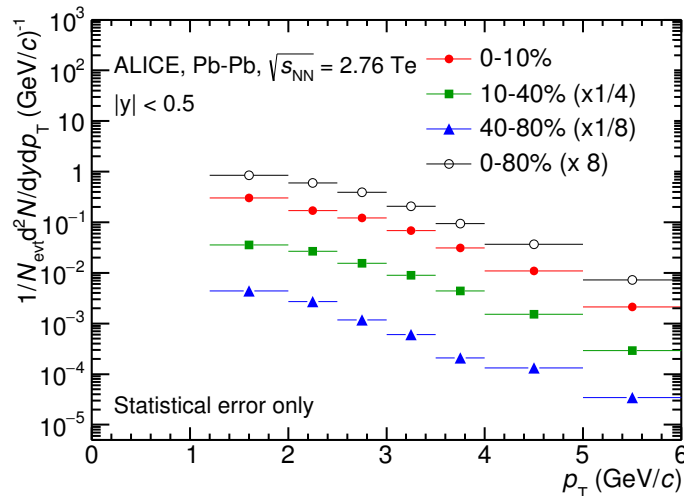


Figure 27: Corrected p_T -spectra of $\Xi(1530)^0$ in different centrality classes in Pb-Pb collisions.

483 **5.4 Systematic uncertainties**

484 The systematic uncertainties are calculated in seven principle groups. The procedure to ob-
485 tain the systematic uncertainties is performed many times by varying the possible permuta-
486 tion of the analysis parameter. The general strategy for evaluating systematic uncertainties
487 is described as following:

- 488 1. Choose one set of parameters for the analysis as default
- 489 2. Observe the deviation of yield when one parameter is changed
- 490 3. The systematic uncertainty is calculated for a given source as the RMS deviation of
491 the available sources.
- 492 4. The total systematic uncertainty, taking into account all the different sources, is the
493 sum in quadrature of each source.

494 To study the systematic effect we repeat the measurement by varying one parameter at
495 a time. A Barlow [21] check has been performed for each measurement to verify whether it
496 is due to a systematic effect or a statistical fluctuation. Let each measurement be indicated
497 by $(y_i \pm \sigma_i)$ and the central value (default measurement) by $(y_c \pm \sigma_c)$, one can define $\Delta\sigma_i$
498 (Eq. 3).

$$\Delta\sigma_i = \sqrt{(|\sigma_i^2 - \sigma_c^2|)} \quad (3)$$

499 Then we calculate $n_i = \Delta y_i / \Delta\sigma_i$, where $\Delta y_i = |y_c - y_i|$. If $n_i \leq 1.0$ then the effects
500 are due to the statistical fluctuation and if $n_i > 1.0$ we apply consistency check. Since
501 the alternate and default measurements are not statistically independent, an alternate
502 measurement which is statistically consistent with the default measurement should not be
503 used in calculating a systematic uncertainty. The difference between the two measurements
504 is $\Delta = y_c - y_i$. The difference in quadrature of the uncertainties is calculated by Eq. 3. It
505 could be possible to check if $\Delta < \sigma$ and exclude such cases from the systematic uncertainties.
506 However, there can be statistical fluctuations for which $\Delta > \sigma$. If the variations between the
507 default and alternate measurements are purely statistical, the distribution of Δ/σ should
508 be a Gaussian with a mean value that is consistent with zero and a deviation σ consistent
509 with unity. In this analysis, if the mean value is less than 0.1 and σ is less than 1, the
510 variation passes the consistency check.

511 Only the measurements which passed the Barlow check ($n_i > 1$) are used to determine
512 the systematic uncertainty. For measurements $N > 2$, the systematic uncertainty has been
513 determined as the RMS (eqn. 4) of the available measurements. If $N=2$, the absolute
514 difference is assigned as systematic uncertainty.

$$\delta y_{syst.} = \sqrt{\frac{1}{N} \sum_i (y_i - \bar{y})^2} \quad (4)$$

515 Here N is the total number of available measurements including y_c and \bar{y} is the average
516 of value of the measurements. The measurement did not pass Barlow check, zero systematic
517 uncertainty has been assigned to the value.

518 By suing the way as explained above, all the main contributions to the systematic un-
519 certainty of particle spectra have been studied. In particular those that comes from signal
520 extraction, topological and kinematical selection cuts, track quality selection and $n\sigma$ TPC
521 PID variation. the meaning of each source of systematic uncertainty studied is described
522 in the following:

523

524 **Signal extraction**

525 We have extracted the signal with varying the yield calculating method which contains
526 the method of signal extraction by integrating the Voigtian fit function and bin counting.
527 We also have varied the normalisation range which is related to the invariant mass region
528 where the mixed events distribution is scaled to subtract the combinatorial background
529 and different background estimator such as Like-Sign distribution and polynomial fit was
530 taken account into the systematic source of signal extraction. The systematic uncertainty
531 from signal extraction is sum in quadrature of three sources.

532

533 **Topological selection**

534 To evaluate the stability of the chosen set of values for the topological cuts, loose and tight
535 cuts have beed defined in order to vary by $\pm 10\%$ respectively. The parameters are changed
536 once at a time. Total systematic uncertainty from topological selection is calculated by
537 summation in quadrature of nine sources.

538

539 **TPC $N_{cluster}$ selection**

540 The selection performed for the daughter tracks of the cascade is that $N_{cluster}$ is larger
541 than 70 and the value has been varied to 60 and 80 in order to estimate the systematic
542 uncertainty due to this selection.

543

544 **TPC dE/dx selection**

545 In order to evaluate any potential effect due to the TPC dE/dx selection (U_{PID}), the N_σ
546 selection was varied with $N = 2.5$ and 3.5 .

547

548 **p_T shape correction**

549 As described in Section 5.2, due to the different shape of the measured and generated
550 $\Xi(1530)^0$ spectra, we have applied reweighing procedure to the generated spectra to have
551 same shape and this correction is added into contributor of systematic uncertainty as
552 p_T shape correction.

553

554 **Mass window range selection**

555 In order to select Ξ^\pm which is daughter particle of $\Xi(1530)^0$, we apply the mass window

556 ± 7 MeV/ c^2 around $\Xi(1530)^0$ mass on $\Lambda\pi$ invariant mass distribution. The boundaries
557 has been varied to ± 6 MeV/ c^2 and ± 8 MeV/ c^2 to estimate systematic uncertainty.

558

559 **Vertex range selection**

560 The distribution of vertex-z is shown in Fig.3. The cut on $|Vz|$ was varied from the nominal
561 ± 10 cm to ± 9 cm, ± 11 cm.

562

563 **Material Budget and hadronic cross section**

564 A possible source of uncertainty comes from the description of the material, active (de-
565 tecting area) or dead (structure and cable), that the particles cross during their travel in
566 the MC with respect to the real material present in the detector. Such description could
567 affect the reconstruction efficiency in different aspects (e.g. multiple scattering, energy
568 loss). The value estimated by Ξ analysis [22] has been used in this study which gives 4%
569 systematic uncertainty. In case of systematic uncertainty from hadronic cross section, we
570 have inherited the value studied in previous measurement[23] which amount is 1%.

571

572 **Tracking efficiency**

573 Systematic uncertainties from tracking efficiency from ITS + TPC combined track were
574 assigned as 3% in p–Pb and 4% in Pb–Pb collision system.[23]

575 (<https://twiki.cern.ch/twiki/bin/view/ALICE/TrackingEfficiencyCharged>)

576

577 Finally, total systematic uncertainty is sum in quadrature of sources listed above. Fig-
578 ure 28 and Figure 29 show the total systematic uncertainty in minimum bias event and
579 different multiplicity classes in p–Pb collisions, respectively. Again, Figure 30 and Figure
580 31 present the total systematic uncertainty in minimum bias event and different centrality
581 classes in Pb–Pb collisions.

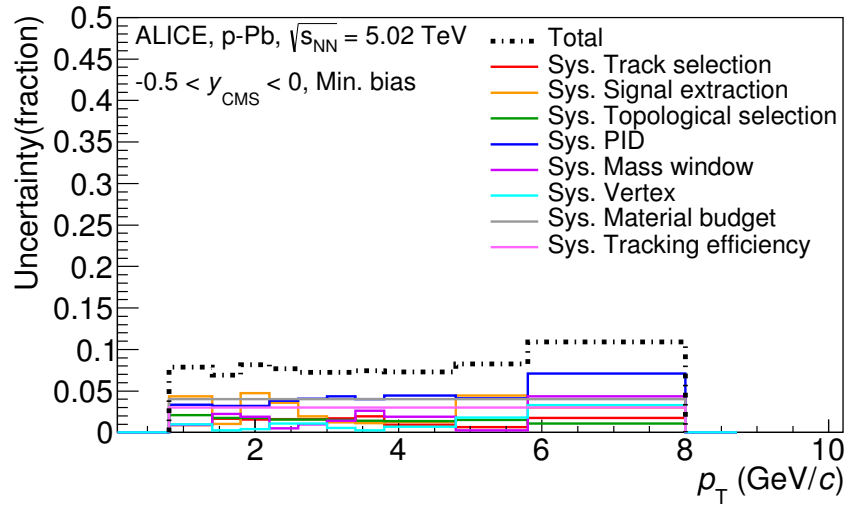


Figure 28: Summary of the contributions to the systematic uncertainty in minimum bias events in p–Pb collisions. The dashed black line is the sum in quadrature of all the contributions.

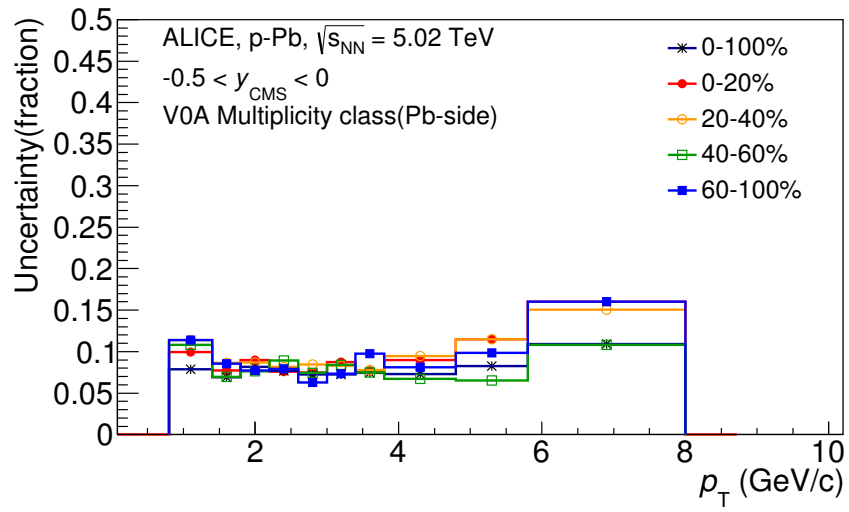


Figure 29: Systematic uncertainties for each multiplicity classes in p–Pb collisions.

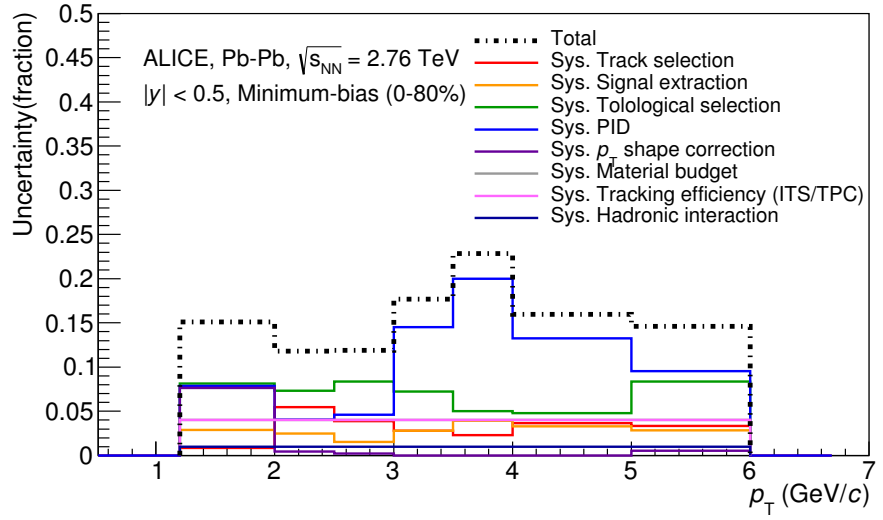


Figure 30: Summary of the contributions to the systematic uncertainty in minimum bias events in Pb–Pb collisions. The dashed black line is the sum in quadrature of all the contributions.

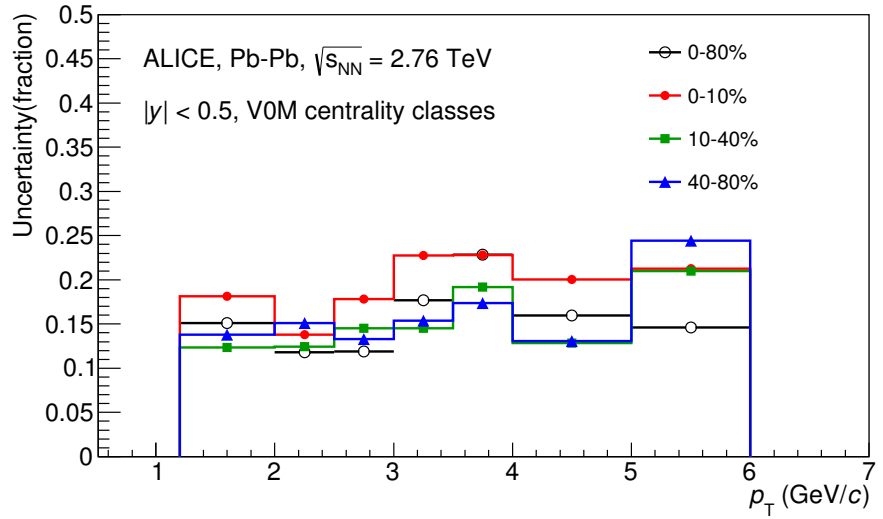


Figure 31: Systematic uncertainties for each multiplicity classes.

Source of uncertainty	p-Pb	Pb-Pb
<i>p</i> _T -dependent		
Tracking efficiency	3%	4%
Tracks selection	1-2%	1-5%
Topological selection	1-2%	5-8%
PID	3-7%	4-20%
Signal extraction	1-5%	1-4%
<i>p</i> _T shape correction	-	0-8%
Mass window (Ξ^\pm)	4%	-
Vertex selection	3%	-
<i>p</i> _T -independent		
Hadronic interaction	-	1%
Material budget	4%	4%
Branching ratio	0.3%	0.3%
Total	8-12%	9-25 %

Table 7: Summary of the systematic uncertainties on the differential yield, $d^2N/(dp_T dy)$. Minimum and maximum values in all p_T intervals and multiplicity classes in p–Pb, centrality classes in Pb–Pb are shown for each source.

582 **5.5 $\Xi(1530)^0$ transverse momentum spectra**

583 The raw yield shown in Figure 26 and 27 have been corrected for efficiency as described
 584 in section 5.2. The measured spectra for $(\Xi(1530)^0 + \bar{\Xi}(1530)^0)/2$ are reported in Figure
 585 32 for p–Pb collisions and Figure 33 for Pb–Pb collisions. The statistical and systematic
 586 uncertainties are reported respectively as the error bars and the boxes on the plot. The
 587 corrected yields for p–Pb collisions are measured with $0.8 < p_T < 8.0$ GeV/c while the
 588 yields for Pb–Pb collisions are obtained with $1.2 < p_T < 6.0$ GeV/c due to difficulty of
 589 signal extraction in low and high p_T region.

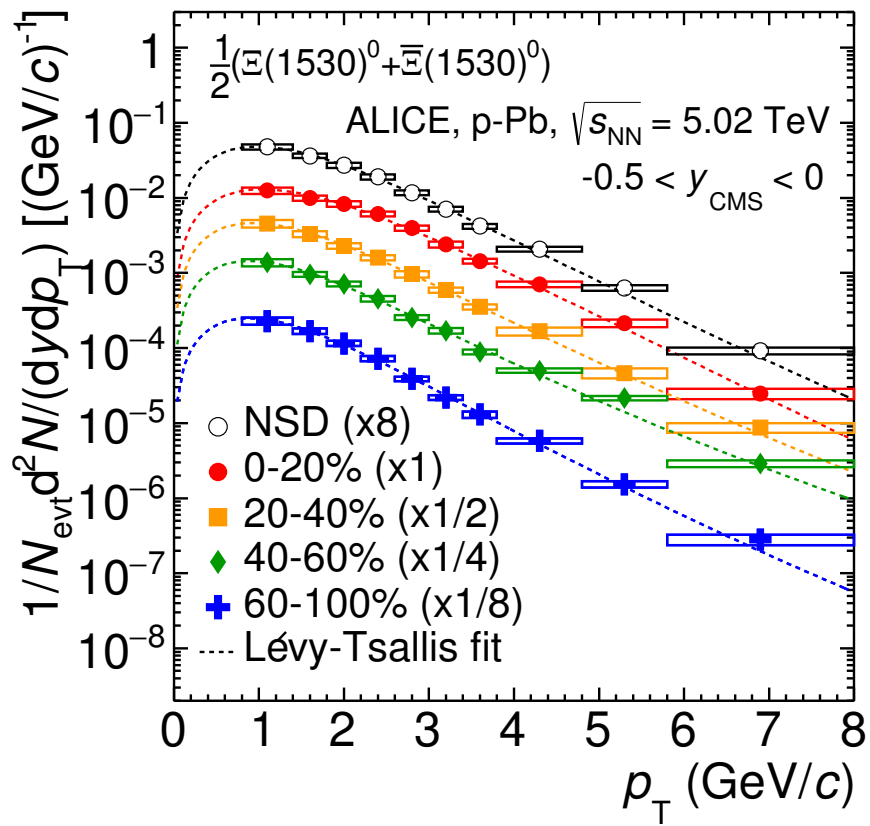


Figure 32: Corrected yields as function of p_T in NSD events and multiplicity dependent event classes in p-Pb collision system. Statistical uncertainties are presented as bar and systematical uncertainties are plotted as boxes.

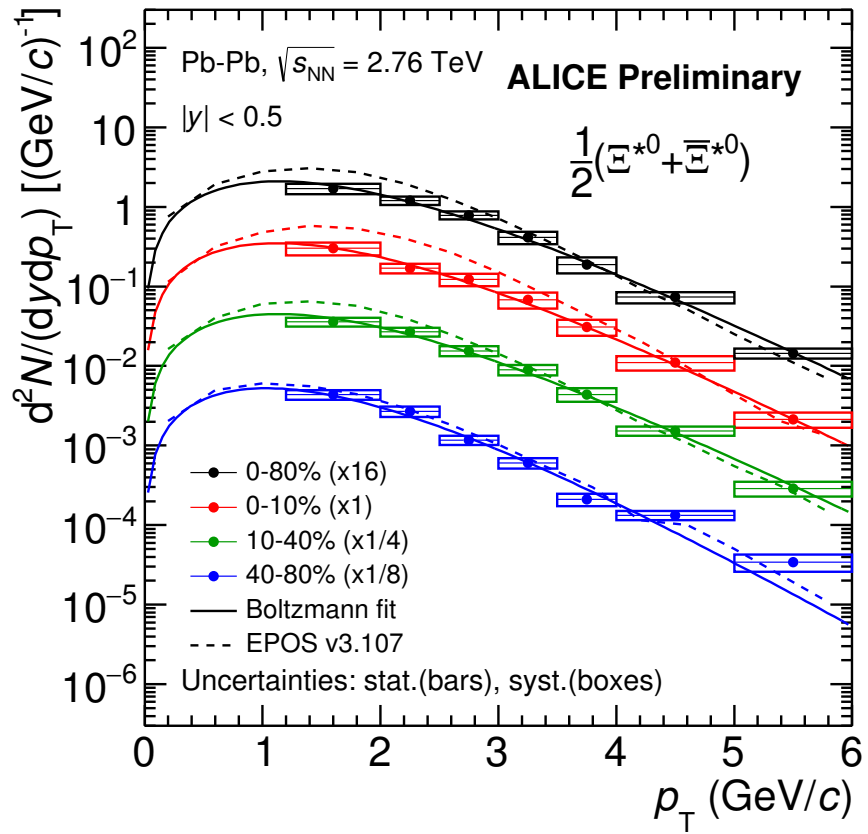


Figure 33: Corrected yields as function of p_T in different centrality classes in Pb-Pb collision system. Statistical uncertainties are presented as bar and systematical uncertainties are plotted as boxes.

590 **6 Further results and discussion**

591 The transverse momentum distributions of double-strange hyperon resonances, $\Xi(1530)^0$
592 , produced in p–Pb collisions at $\sqrt{s_{\text{NN}}}= 5.02$ TeV and Pb–Pb collisions at $\sqrt{s_{\text{NN}}}= 2.76$
593 TeV were measured in the mid-rapidity range and they have been already presented in
594 Chapter 5. From the measurement, the $\langle p_{\text{T}} \rangle$ and integrated particle yield ratios with
595 system size have been obtained. In the present Chapter these results are compared with
596 model predictions and discussed in connection with the following topics:

- 597
 - Mean transverse momentum studies
 - 598 • Study of particle production mechanism in hadronic phase
 - 599 • Study of strangeness enhancement

600 Most of the theoretical aspects related to these topics and, in particular, the description
601 of the models already have been addressed in Chapter 3.

602 **6.1 Mean transverse momentum**

603 Figure 34 shows the mean transverse momentum $\langle p_{\text{T}} \rangle$ as a function of mean charged-
604 particle multiplicity density $\langle dN_{\text{ch}}/d\eta_{\text{lab}} \rangle$ at midrapidity. The results for $\Xi(1530)^0$ are
605 compared with those for other hyperons observed in p–Pb collisions at $\sqrt{s_{\text{NN}}}= 5.02$ TeV [1,
606 3].

607 Increasing trends from low to high multiplicities are observed for all hyperons. The
608 mean transverse momenta increase by 20% as the mean charged-particle multiplicity in-
609 creases from 7.1 to 35.6. This result is similar to the one obtained for the other hyperons.
610 Furthermore, a similar increase has been observed also for K^{\pm} , K_S^0 , $K^*(892)^0$ and ϕ [2],
611 whereas protons are subject to a larger ($\sim 33\%$) increase in the given multiplicity range,
612 as discussed also in Ref. [1].

613 In all multiplicity classes, the $\langle p_{\text{T}} \rangle$ follows an approximate mass ordering:

- 614
 - $\langle p_{\text{T}} \rangle_{\Lambda} < \langle p_{\text{T}} \rangle_{\Xi^-} \simeq \langle p_{\text{T}} \rangle_{\Sigma^{*\pm}} < \langle p_{\text{T}} \rangle_{\Xi^{*0}} < \langle p_{\text{T}} \rangle_{\Omega^-}$

615 The $\langle p_{\text{T}} \rangle$ of $\Sigma^{*\pm}$ looks systematically lower than the $\langle p_{\text{T}} \rangle$ of Ξ^- , despite the larger mass
616 of $\Sigma^{*\pm}$. The uncertainties, however, are too large to draw any conclusion on possible hints
617 of violation of the mass hierarchy. This hierarchy of mass-ordering, also including D^0 and
618 J/ψ in the comparison, is displayed in Figure 35. Note, however, that the D^0 and J/ψ
619 were measured in different rapidity ranges: $|y_{\text{CMS}}| < 0.5$ [5] ($|y_{\text{CMS}}| < 0.9$ [6]) for D^0 (J/ψ)
620 in pp and $-0.96 < y_{\text{CMS}} < 0.04$ [5] ($-1.37 < y_{\text{CMS}} < 0.43$ [7]) for D^0 (J/ψ) in p–Pb, and
621 the results for D^0 and J/ψ in p–Pb collisions are for the 0-100% multiplicity class. This
622 mass dependence is observed in both p–Pb and pp collisions. It was observed also by the
623 STAR collaboration [24] in MB pp, MB d–Au and central Au–Au collisions.

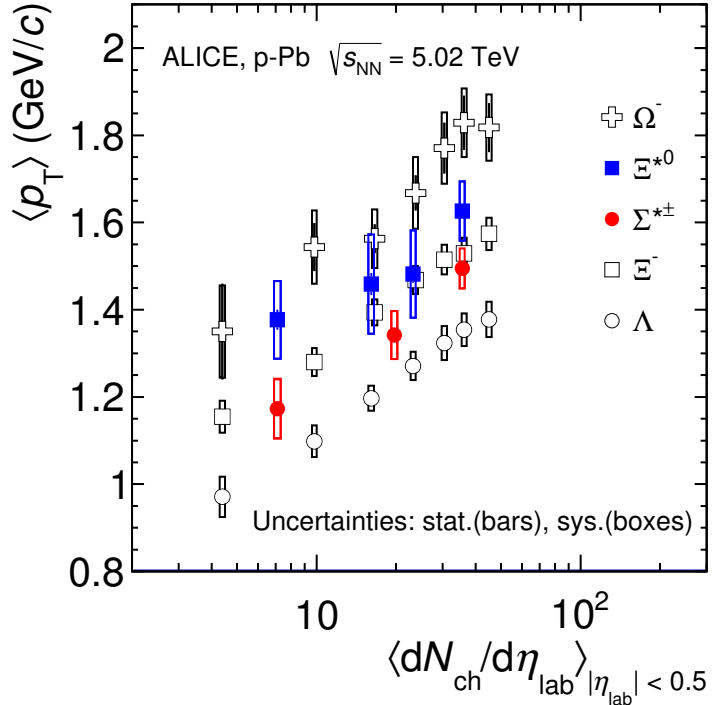


Figure 34: Mean transverse momenta $\langle p_T \rangle$ of Λ , Ξ^- , $\Sigma^{*\pm}$, Ξ^{*0} and Ω^- in p–Pb collisions at $\sqrt{s_{NN}}=5.02$ TeV as a function of mean charged-particle multiplicity density $\langle dN_{ch}/d\eta_{lab} \rangle$, measured in the pseudorapidity range $|\eta_{lab}| < 0.5$. The results for Λ , Ξ^- and Ω^- are taken from [1, 2, 3]. Statistical and systematic uncertainties are represented as bars and boxes, respectively. The Ω^- and Ξ^- points in the 3rd and 4th lowest multiplicity bins are slightly displaced along the abscissa to avoid superposition with the $\Xi(1530)^0$ points.

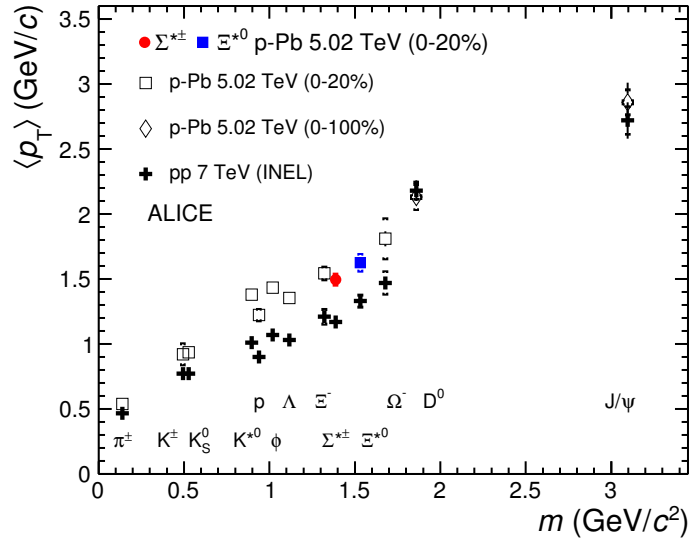


Figure 35: Mass dependence of the mean transverse momenta of identified particles for the 0 – 20% V0A multiplicity class and with $-0.5 < |y_{\text{CMS}}| < 0$ in p–Pb collisions at $\sqrt{s_{\text{NN}}} = 5.02$ TeV [1, 3], and in minimum-bias pp collisions at $\sqrt{s} = 7$ TeV [4] with $|y_{\text{CMS}}| < 0.5$. Additionally, D^0 and J/ψ results are plotted. The D^0 and J/ψ were measured in different rapidity ranges: $|y_{\text{CMS}}| < 0.5$ [5] ($|y_{\text{CMS}}| < 0.9$ [6]) for D^0 (J/ψ) in pp and $-0.96 < |y_{\text{CMS}}| < 0.04$ [5] ($-1.37 < |y_{\text{CMS}}| < 0.43$ [7]) for D^0 (J/ψ) in p–Pb. Note also that the results for D^0 and J/ψ in p–Pb collisions are for the 0–100% multiplicity class.

624 Furthermore, for the light-flavour hadrons, the mean transverse momenta in p–Pb col-
625 lisions are observed to be consistently higher than those in pp collisions at 7 TeV. The
626 situation for the charm hadrons is different, where $\langle p_T \rangle$ appears compatible between both
627 colliding systems. The discrepancy is likely due to different production mechanisms for
628 heavy and light flavours and to a harder fragmentation of charm quarks. Specifically, the
629 fact that $\langle p_T \rangle$ remains similar in pp and in p–Pb is consistent with an $R_{p\text{Pb}}$ ratio com-
630 patible with unity at all p_T [5] for D^0 , and/or with the effects of shadowing in p–Pb which
631 reduces the production at low p_T and thus increasing the overall $\langle p_T \rangle$ for J/ψ [7]; the small
632 p_T hardening expected in pp when going from 5.02 to 7 TeV is apparently not enough to
633 counter-balance the situation.

634 Because of small decrease of the $\langle p_T \rangle$ for proton and Λ relative to those for K^{*0} and
635 ϕ , two different trends for mesons and baryons have been suggested [25]. Even including
636 D^0 and J/ψ , as shown in Figure 35, a different trend for mesons and baryons cannot be
637 convincingly established.

638 **6.2 Particle yield ratios**

639 **6.2.1 Integrated yield ratios of excited to ground-state hadrons**

640 The integrated yield ratios of excited to ground-state hyperons [26, 1, 4, 3] with the same
641 strangeness content, for different collision systems and energies, are shown in Figure 36
642 as a function of system size. The ratio of $\Xi(1530)^0$ to Ξ is flat across the system and
643 it complements the information derived from other resonance measurement for different
644 lifetime which are shown in Figure 37.

645 The short-lived resonances(ρ , K^* and Λ^*) which exhibit suppression from peripheral to
646 central lead-lead collisions and with respect to thermal model in central lead-lead collisions.
647 Currently favored explanation of is dominance of elastic re-scattering of decay daughters
648 over regeneration in the hadronic phase.

649 The constant behavior of the yield ratios of excited to ground-state hyperons with same
650 strangeness content ($\Xi(1530)^0$ and Φ) indicates that neither regeneration nor re-scattering
651 dominates with increasing collision system size because of its longer-lifetime.

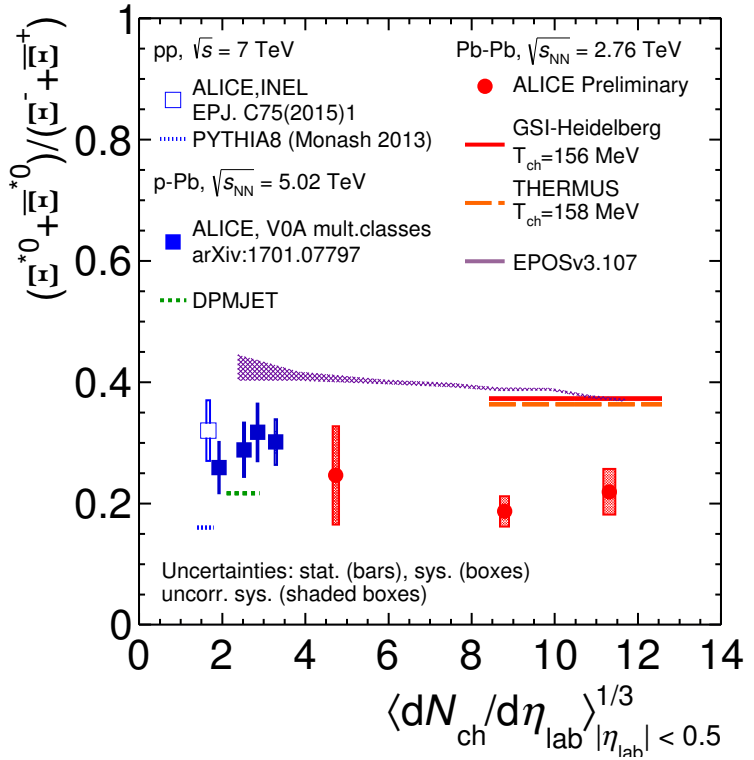


Figure 36: Ratio of $\Xi(1530)^0$ to Ξ^- measured in pp [4], p–Pb [1, 3] and Pb–Pb collisions as a function of $\langle dN_{ch}/d\eta_{lab} \rangle$ measured at midrapidity. Statistical uncertainties (bars) are shown as well as total systematic uncertainties (hollow boxes) and systematic uncertainties uncorrelated across multiplicity (shaded boxes). A few model predictions are also shown as lines at their appropriate abscissa.

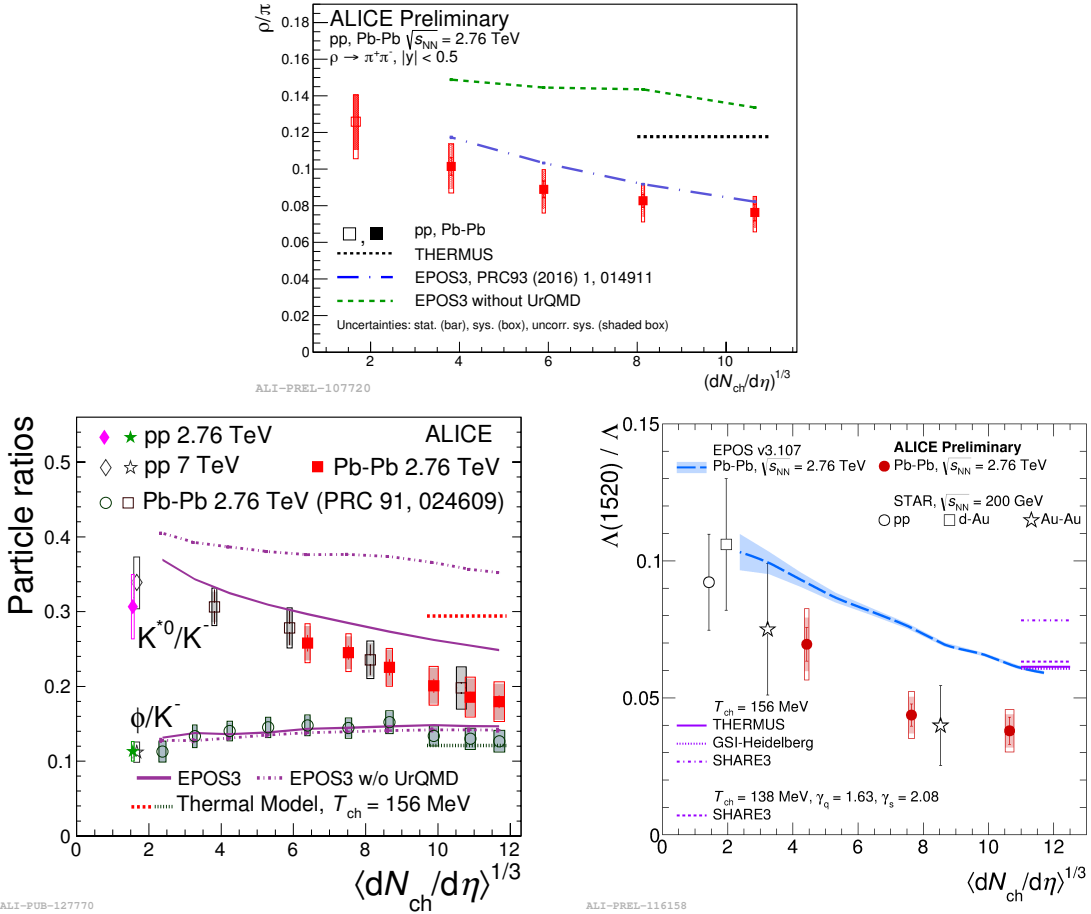


Figure 37: Ratio of ρ/π (Up), K^*/K , ϕ/K (Left bottom) and Λ^*/Λ with system size measured at mid-rapidity. Statistical uncertainties (bars) are shown as well as total systematic uncertainties (hollow boxes) and systematic uncertainties uncorrelated across multiplicity (shaded boxes). A few model predictions are also shown as lines at their appropriate abscissa.

652 **6.3 Integrated yield ratios to pion**

653 The integrated yield ratios of excited hyperons to pions are shown in Figure 38 to study
654 the evolution of relative strangeness production yields with increasing collision system
655 size. The ratio of $\Xi(1530)^0$ to Ξ is observed to be increase from pp to p–Pb collisions
656 system and then, decrease from peripheral to central Pb–Pb collision. The QCD-inspired
657 predictions like PYTHIA for pp [27] and DPMJET for p–Pb [19] clearly underestimate
658 the observed yield ratios, while the statistical one seems to be comparable with results
659 from high multiplicity in p–Pb but the ratio in Pb–Pb is below with respect to the model.
660 The results in pp and p–Pb collisions are consistent with previous observation of ground-
661 state hyperons to pion ratios. The Figure 39 presents particle yield ratios to pions of
662 strange and multi-strange hadrons normalized to the values measured in pp collisions. As
663 shown in the Figure 39, the $\Xi(1530)^0$ to pion ratios follow the trend of $\Xi \pi$ as function of
664 $\langle dN_{ch}/d\eta_{lab} \rangle$ and indicate that the strangeness enhancement observed in p–Pb collisions
665 depends predominantly on the strangeness content, rather than on the hyperon mass.

666 The Figure 40 also shows the hyperon-to-pion ratios and compared with model predic-
667 tions. The

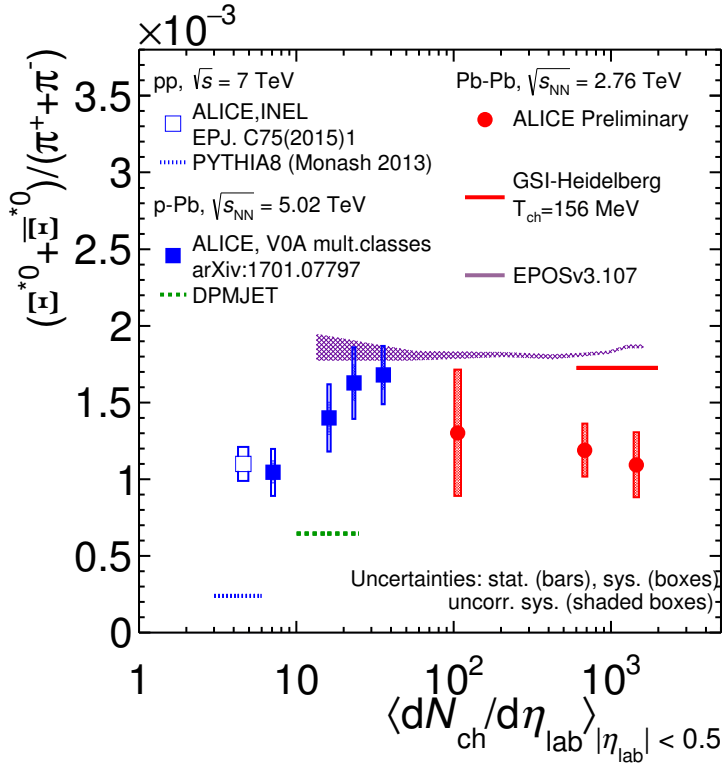


Figure 38: Ratio of $\Xi(1530)^0$ to π^\pm , measured in pp [8] and p–Pb [4] collisions, as a function of the average charged particle density ($\langle dN_{\text{ch}}/d\eta_{\text{lab}} \rangle$) measured at mid-rapidity. Statistical uncertainties (bars) are shown as well as total systematic uncertainties (hollow boxes) and systematic uncertainties uncorrelated across multiplicity (shaded boxes). A few model predictions are also shown as lines at their appropriate abscissa.

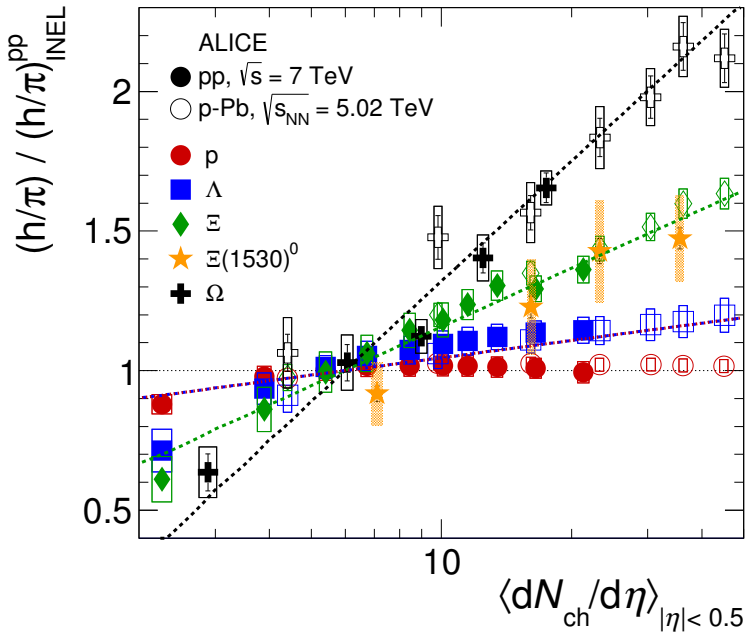


Figure 39: Particle yield ratios to pions of strange and multi-strange hadrons normalized to the values measured in pp collisions, both in pp and in p–Pb collisions. The common systematic uncertainties cancel in the double-ratio. The empty boxes represent the remaining uncorrelated uncertainties. The lines represent a simultaneous fit of the results with the empirical scaling formula in Equation ??.

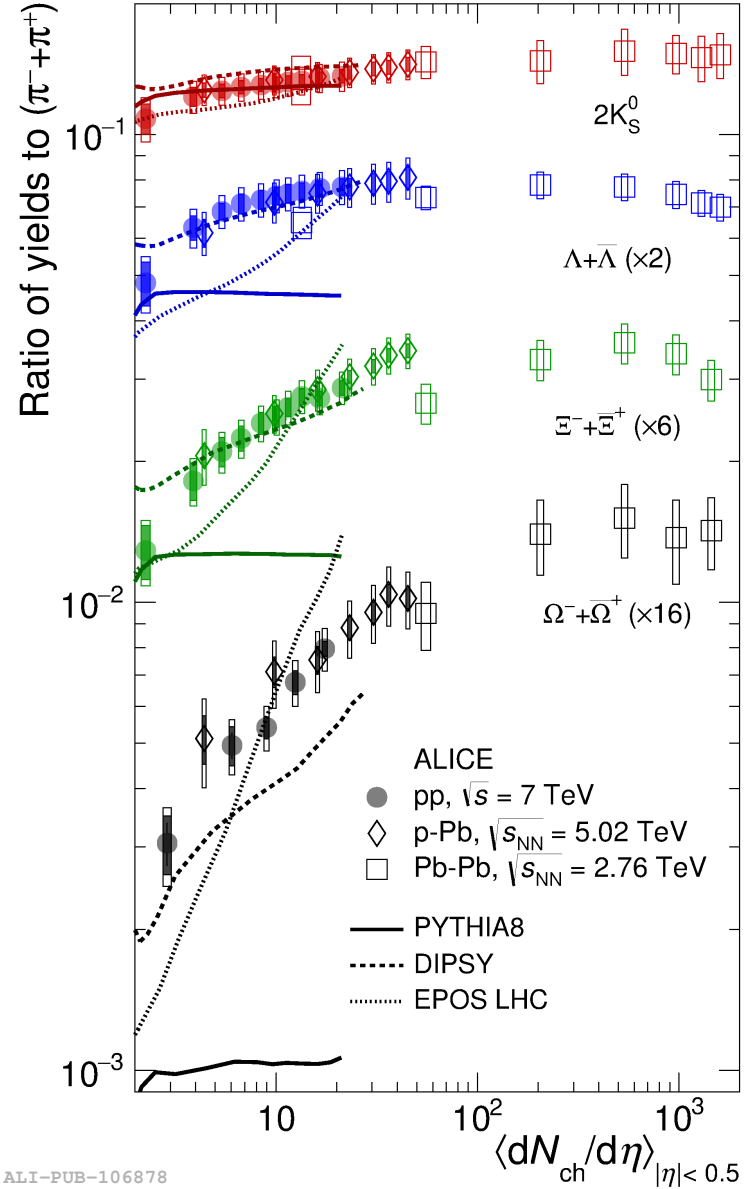


Figure 40: p_T -integrated yield ratios of strange and multi-strange hadrons to $(\pi^+ + \pi^-)$ as a function of $\langle dN_{\text{ch}} / d\eta_{\text{lab}} \rangle$ measured in the rapidity interval $|\eta| < 0.5$. The empty and dark-shaded boxes show the total systematic uncertainty and the contribution uncorrelated across multiplicity bins, respectively. The values are compared to calculations from MC models and to results obtained in Pb–Pb and p–Pb collisions at the LHC.

668 **References**

- 669 [1] **ALICE** Collaboration, J. Adam *et al.*, “Multiplicity dependence of pion, kaon,
670 proton and lambda production in p–Pb collisions at $\sqrt{s_{\text{NN}}}= 5.02 \text{ TeV}$,” *Phys. Lett.*
671 **B728** (2014) 25–38, [arXiv:1307.6796 \[nucl-ex\]](#).
- 672 [2] **ALICE** Collaboration, J. Adam *et al.*, “Production of $K^*(892)^0$ and $\phi(1020)$ in
673 p–Pb collisions at $\sqrt{s_{\text{NN}}}= 5.02 \text{ TeV}$,” *Eur. Phys. J.* **C76** (2016) 245,
674 [arXiv:1601.7868 \[nucl-ex\]](#).
- 675 [3] **ALICE** Collaboration, J. Adam *et al.*, “Multi-strange baryon production in p–Pb
676 collisions at $\sqrt{s_{\text{NN}}}=5.02 \text{ TeV}$,” *Phys. Lett.* **B758** (2016) 389–401,
677 [arXiv:1512.07227 \[nucl-ex\]](#).
- 678 [4] **ALICE** Collaboration, B. Abelev *et al.*, “Production of $\Sigma(1385)^{\pm}$ and $\Xi(1530)^0$ in
679 proton-proton collisions at $\sqrt{s}= 7 \text{ TeV}$,” *Eur. Phys. J.* **C75** (2015) 1,
680 [arXiv:1406.3206 \[nucl-ex\]](#).
- 681 [5] **ALICE** Collaboration, J. Adam *et al.*, “ D -meson production in p–Pb collisions at
682 $\sqrt{s_{\text{NN}}}= 5.02 \text{ TeV}$ and in pp collisions at $\sqrt{s}= 7 \text{ TeV}$,” *Phys. Rev. C* **94** (2016)
683 054908, [arXiv:1605.07569 \[nucl-ex\]](#).
- 684 [6] **ALICE** Collaboration, B. Abelev *et al.*, “Inclusive J/ψ production in pp collisions
685 at $\sqrt{s}= 2.76 \text{ TeV}$,” *Phys. Lett.* **B718** (2012) 295–306, [arXiv:1203.3641 \[hep-ex\]](#).
- 686 [7] **ALICE** Collaboration, J. Adam *et al.*, “Rapidity and transverse-momentum
687 dependence of the inclusive J/ψ nuclear modification factor in p–Pb collisions at
688 $\sqrt{s_{\text{NN}}}= 5.02 \text{ TeV}$,” *JHEP* **06** (2015) 55, [arXiv:1503.07179 \[nucl-ex\]](#).
- 689 [8] **ALICE** Collaboration, J. Adam *et al.*, “Measurement of pion, kaon and proton
690 production in proton-proton collisions at $\sqrt{s} = 7 \text{ TeV}$,” *Eur. Phys. J.* **C75** (2015)
691 226, [arXiv:1504.00024 \[nucl-ex\]](#).
- 692 [9] D. Hahn and H. Stoecker, “THE QUANTUM STATISTICAL MODEL OF
693 FRAGMENT FORMATION: ENTROPY AND TEMPERATURE EXTRACTION
694 IN HEAVY ION COLLISIONS,” *Nucl. Phys.* **A476** (1988) 718–772.
- 695 [10] S. Wheaton, J. Cleymans, and M. Hauer, “THERMUS: A Thermal model package
696 for ROOT,” *Comput. Phys. Commun.* **180** (2009) 84–106, [hep-ph/0407174](#).
- 697 [11] J. Cleymans, S. Kabana, I. Kraus, H. Oeschler, K. Redlich, and N. Sharma,
698 “Antimatter production in proton-proton and heavy-ion collisions at ultrarelativistic
699 energies,” *Phys. Rev.* **C84** (2011) 054916, [arXiv:1105.3719 \[hep-ph\]](#).
- 700 [12] L. Evans and P. Bryant.

- 701 [13] **ALICE** Collaboration, K. Aamodt *et al.*, “The ALICE experiment at the CERN
 702 LHC,” *JINST* **3** (2008) S08002.
- 703 [14] **ALICE** Collaboration, B. Abelev *et al.*, “Performance of the ALICE Experiment at
 704 the CERN LHC,” *Int. J. Mod. Phys. A* **29** (2014) 1430044, [arXiv:1402.4476](#)
 705 [nucl-ex].
- 706 [15] **ALICE** Collaboration, B. Abelev *et al.*, “Pseudorapidity Density of Charged
 707 Particles in p–Pb Collisions at $\sqrt{s_{\text{NN}}}= 5.02$ TeV,” *Phys. Rev. Lett.* **110** (2013)
 708 032301, [arXiv:1210.3615](#) [nucl-ex].
- 709 [16] **ALICE** Collaboration, B. Abelev *et al.*, “Centrality determination of Pb–Pb
 710 collisions at $\sqrt{s_{\text{NN}}}= 2.76$ TeV with ALICE,” *Phys. Rev. C* **88** (2013) ,
 711 [arXiv:1303.0737](#) [nucl-ex].
- 712 [17] **Particle Data Group** Collaboration, K. Olive *et al.*, “Review of Particle Physics,”
 713 *Chin. Phys. C* **38** (2014) 090001.
- 714 [18] **ALICE** Collaboration, K. Aamodt *et al.*, “Strange particle production in
 715 proton-proton collisions at $\sqrt{s}= 0.9$ TeV with ALICE at the LHC,” *Eur. Phys. J. C*
 716 **71** (2011) 1594, [arXiv:1012.3257](#) [nucl-ex].
- 717 [19] S. Roesler, R. Engel, , and J. Ranft, “The Monte Carlo Event Generator
 718 DPMJET-III, Advanced Monte Carlo for Radiation Physics, Particle Transport
 719 Simulation and Applications,” *Conference Proceedings, MC2000, Lisbon, Portugal,*
 720 *October 23-26* (2000) 1033–1038, [hep-ph/0012252](#).
- 721 [20] R. Brun, F. Carminati, and S. Giani, “GEANT detector description and simulation
 722 tool,” *CERN-W5013* (1994) .
- 723 [21] R. Barlow, “Systematic Errors: Facts and Fictions,” *Presented at Advanced
 724 Statistical Techniques in HEP, Durham, March 2002* (2002) 333p,
 725 [hep-ex/0207026v1](#).
- 726 [22] **ALICE** Collaboration, B. Abelev *et al.*, “Multi-strange baryon production at
 727 mid-rapidity in Pb–Pb collisions at $\sqrt{s_{\text{NN}}}= 2.76$ TeV,” *Phys. Lett. B* **728** (2014)
 728 216–227, [arXiv:1307.5543](#) [nucl-ex].
- 729 [23] **ALICE** Collaboration, B. Abelev *et al.*, “Centrality dependence of π , K and p
 730 production in Pb–Pb collisions at $\sqrt{s_{\text{NN}}}= 2.76$ TeV,” *Phys. Rev. C* **88** (2013) ,
 731 [arXiv:1301.4361](#) [nucl-ex].
- 732 [24] **STAR** Collaboration, B. I. Abelev *et al.*, “Hadronic resonance production in d–Au
 733 collisions at $\sqrt{s_{\text{NN}}}= 200$ GeV measured at the BNL Relativistic Heavy-Ion Collider,”
 734 *Phys. Rev. C* **78** (2008) 044906, [arXiv:0801.0450](#) [nucl-ex].

- 735 [25] A. Velásquez, “Mean p_T scaling with m/n_q at the LHC: Absence of (hydro) flow in
736 small systems?,” *Nucl. Phys.* **A943** (2015) 9–17, arXiv:1506.00584 [hep-ph].
- 737 [26] **ALICE** Collaboration, B. Abelev *et al.*, “Multi-strange baryon production in pp
738 collisions at $\sqrt{s}= 7$ TeV with ALICE,” *Phys. Lett.* **B712** (2012) 309,
739 arXiv:1204.0282 [nucl-ex].
- 740 [27] T. Sjöstrand, S. Mrenna, and P. Skands, “A brief introduction to PYTHIA 8.1,”
741 *Comput. Phys. Comm.* **178** (2008) 852–867, arXiv:0710.3820 [hep-ph].

742 **Acknowledgements**